OBSERVATION-BASED SEA LEVEL FORECASTS FOR THE HAWAIIAN ISLANDS

A THESIS SUBMITTED TO THE GRADUATE DIVISION OF
THE UNIVERSITY OF HAWAIʻI AT MĀNOA
IN PARTIAL FULFILLMENT OF THE REQUIREMENTS FOR THE DEGREE OF

MASTER OF SCIENCE

IN

OCEANOGRAPHY

MAY 2021

By Hyang Yoon

Thesis Committee:

Philip R. Thompson, Chairperson
Mark A. Merrifield
James T. Potemra
Bo Qiu

Dedicated to my mother

Hyangja Kim

Saranghae!

Acknowledgments

I would like to thank my advisor Philip R. Thompson for his expertise, guidance, and continued patience throughout this project. I would also like to thank the members of my committee Mark A. Merrifield, James T. Potemra, and Bo Qiu for their insight, wisdom, and keeping me on track. I would also like to thank Matthew J. Widlansky for his assistance and knowledge with the ocean and atmospheric dynamical and statistical models. Special thanks Kristin Momohara for all the administrative support that she has provided to a complicated international student like myself. Thank you to the entire oceanography and JIMAR faculty and staff for providing a supportive work environment. Thanks to my oceanography cohort and officemate, Carleigh Vollbrecht, who added so much joy to the journey and encouraged me to stay on course. Finally, I would like to thank my *umma*, brother, and my family and friends, who supported me throughout my oceanography education. I am so lucky to have had support I received from these special people over the years.

Abstract

The Hawaiian Islands experienced record-high sea levels during 2017, which caused nuisance flooding in vulnerable coastal communities, especially when positive sea level anomalies coincided with high tides. To build toward solutions for mitigating inundation risk, the predictability of daily-averaged sea level anomalies is investigated. The investigation focused on leveraging observed westward propagation that open-ocean anomalies exhibit over a range of timescales to make sea level predictions. Daily near-real-time gridded altimetry was used to specify upstream sea level at each site with propagation speeds based on mode-one baroclinic Rossby wave speeds. An optimized observation-based forecast was created from weighted combinations of persistence and independent propagation-based forecasts for large (>300 km) and mesoscale (<300 km) open-ocean anomalies. Skill of the observation-based sea level forecasts exceeds persistence at long lead times out to 180 days. The utility of the observation-based sea level forecast was demonstrated by pairing the mean sea level forecast with a statistical model relating mean sea level to counts of flooding threshold exceedances. The combined model performed well in hindcasting seasonal periods of enhanced high-tide flooding at Hilo, underscoring the benefit of economical seasonal forecasts of mean sea level. Stakeholders can utilize the combined mean sea level and exceedance forecast model to assess flooding risks months in advance for facilitating preparedness across economic and coastal management sectors.

Contents

List of Tables

List of Figures

Chapter 1

Importance of sea level forecasting in Hawaii

Large parts of the Western Pacific, including around the Hawaiian Islands, are experiencing sea level rise (e.g., *Merrifield and Maltrud*, 2011; *Perrette et al.*, 2013). Sea level rise threatens the infrastructure and economies of coastal communities around the Hawaiian Islands (e.g., *Fletcher et al.*, 2010; *Rotzoll and Fletcher*, 2013; *Anderson et al.*, 2015). Moreover, the current Intergovernmental Panel on Climate Change (IPCC) projections indicate sea levels will be 0.28 to 0.98 m above 1986 - 2005 levels by the end of the 21st century (*Church et al.*, 2013). With the continuing long-term sea level rise, these elevated sea levels would increase in occurrence and with extreme events becoming more prominent (e.g., *Fletcher et al.*, 2010; *Thompson et al.*, 2019; *Habel et al.*, 2020; *Taherkhani et al.*, 2020). The predicted increase in sea level would increase the frequency of nuisance flooding events and impact the coastal communities more frequently and severely around the Hawaiian Islands and could become physically and economically detrimental.

In what may be seen as a window into the future of Hawaiian coastlines, the Hawaiian Islands experienced record-high sea levels during the summer of 2017. For example, August 21, 2017 marked the highest sea level recorded by the Honolulu tide gauge in its 115-year operational history (Figure 1.1). More importantly, however, this single event was just one of an unprecedented number of high sea level events during the year. Daily maximum hourly water levels from the Honolulu tide gauge exceeded 35 cm above Mean Higher High Water (MHHW) just 22 times prior to 2017 and never more than four times during a single year.

During 2017, this threshold was exceeded by daily maximum water levels 15 times over a five-month span (*Thompson et al.*, 2019).

The high sea levels produced high-tide flooding in vulnerable coastal communities across the Hawaiian Islands, which generally occurred under fair weather conditions. Despite the lack of wind and rain, impact reports across the Hawaiian Islands included beach erosion, minor wave inundation, and failed drainage infrastructure (*Anderson et al.*, 2019). These events received both local (e.g., *DLNR*, 2017; *HNN*, 2019) and global (e.g., *SankeiBiz*, 2017; *Mori*, 2017) attention due to the notoriety of Hawaiian beaches and the tourism economy they support. The island of Oahu alone received 6.2 million tourists in 2019 from global locations to enjoy the island's coastline and tropical weather (*DBEDT*, 2020). Understanding the processes contributing to the high sea level events during 2017 and the ability to forecast similar periods in the future is essential for ongoing sea-level-rise preparedness efforts. Skillful sea level forecasts would allow stakeholders across public and private domains to better prepare for periods of enhanced risk from high-tide flooding.

The most predictable component of sea level variability is astronomical tides, and stakeholders often rely on tidal predictions to forecast periods of time when high-tide flooding is possible. The term King Tides is often used in this context; it is a non-scientific term used for the one to two highest astronomical tides of the year (*Sea Grant Program*, 2018; *EPA*, 2019). During summer 2017 in Hawaii, NOAA tidal analysis for Honolulu did predict that the highest astronomical tides of the year would occur during this time, but the tides were not predicted to be anomalously high compared to the highest tides of previous years and cannot—in hindsight—account for the unprecedented number of high-tide-flooding events in Hawaii during 2017. Thus, predictions of astronomical tides alone are not sufficient for forecasting short periods (i.e., months to seasons) in Hawaii during which many high-tide flooding events will cluster together in time.

Since astronomical tidal variability alone cannot account for the unprecedented numbers of high-tide flooding events around the Hawaiian Islands during 2017, additional factors

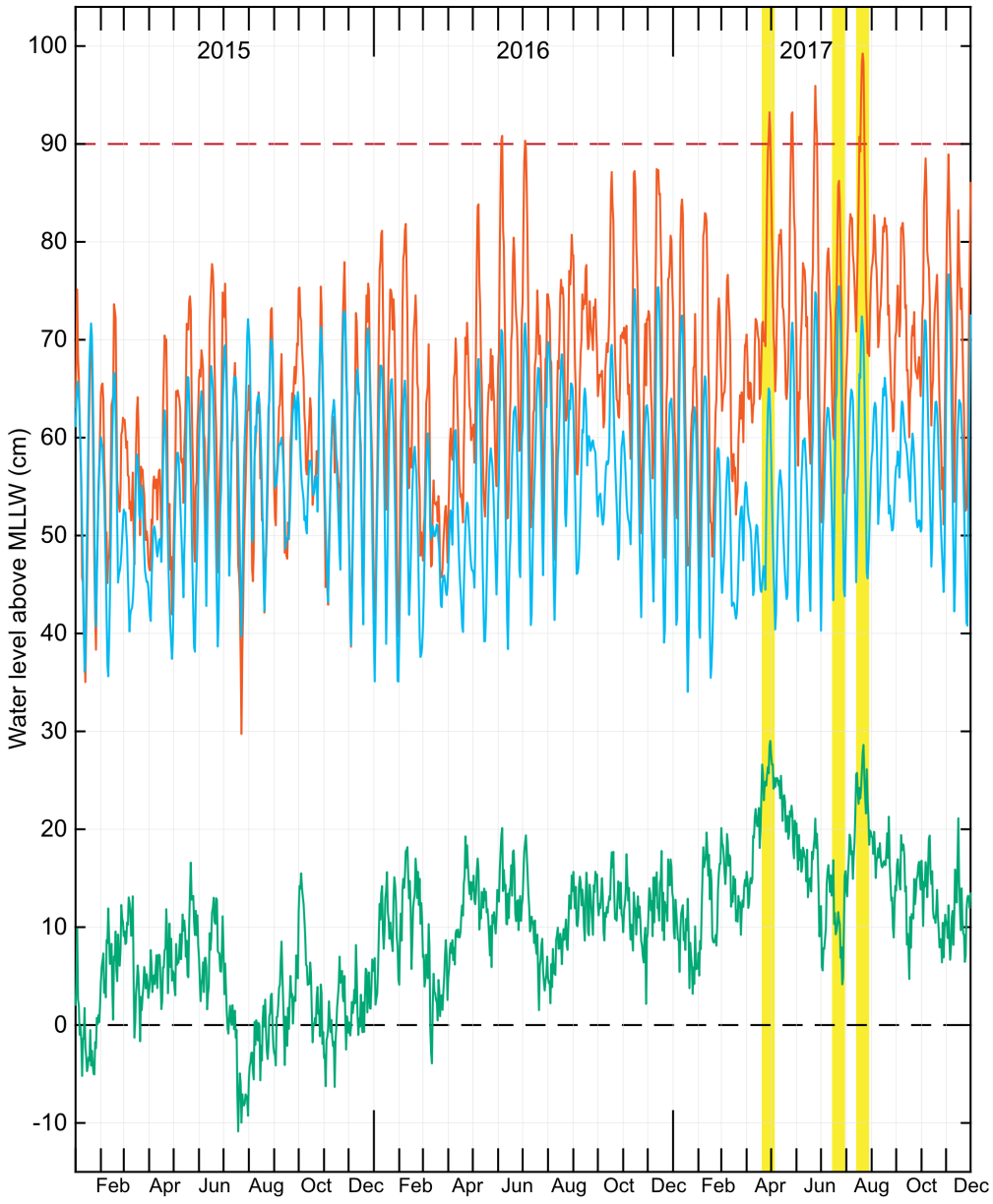

Figure 1.1: Daily maximum hourly sea levels (cm) for Honolulu, HI. Tide predictions (blue) are based on harmonic analysis of the Honolulu Harbor sea level recorded during the NTDE (1983–2001). Predictions and observations (orange) are with respect to the MLLW datum. Residuals between the observed sea levels and the tide prediction are shown by the green line. For reference, the 90 cm water level is shown (dashed horizontal line), which is a threshold for coastal impacts near Honolulu.

must have played a role. Indeed, starting in 2016, the Hawaiian Islands were surrounded by a prolonged positive regional sea level anomaly that propagated westward across the North Pacific, raising sea level around the islands by about 10 cm above normal (*Yoon et al.*, 2018). According to *Long et al.* (2020), the high sea level anomaly was caused by reduced cooling of the surface by anomalously weak trade winds that altered the mixed layer density after an El Niño in 2015.

For the Hawaiian Islands, there are numerous operational statistical and dynamical forecast models available to predict sea level. For the multimodel seasonal sea level forecasts hosted by the University of Hawaii Sea Level Center (UHSLC) (*Widlansky et al.*, 2017), the dynamical forecast models in use are the National Centers for Environmental Prediction (NCEP) coupled forecast system model version 2 (CFSv2) and the Predictive Ocean Atmosphere Model for Australia version 2 (POAMA-2); the statistical models in use are canonical correlation analysis, principal component regression, artificial neural network, and multivariate linear regression. At this time, only two of the models are active in the UHSLC ensemble, the CFSv2 and POAMA-2, which are both models generating dynamical sea level forecasts from fully-coupled operational models. However, there are barriers and limitations with the currently available forward models for sea level forecasts. For instance, the dynamical models, such as the CFSv2, are relatively coarse at the latitude of Hawaii (1° spatial resolution) compared to mesoscale structures in observed sea surface height from the altimetry data. Overall, at higher latitudes, including Hawaii, substantial mesoscale variability associated with instability and geostrophic turbulence inhibits the skill of these models. In addition, dynamical forecast models of the type used in the UHSLC ensemble were primarily developed to generate seasonal climate forecasts and focus on ocean variables such as the sea surface temperature that provide essential boundary conditions for atmospheric variability. For this reason, most of these dynamical models do not assimilate sea surface height data. Regardless, there are a few models that do assimilate the sea surface height, such as those operated at European Centre for Medium-Range Weather Forecasts (ECMWF), but the ad-

dition of sea surface height does not significantly enhance the skill of sea level forecasts at seasonal time scales (personal communication with M. Widlansky).

To address the lack of skill in forecasting sea level using operational dynamical models, the analysis that follows outlines the development of an observation-based seasonal sea level forecast for the Hawaiian Islands. This comparatively simple approach prioritizes the initial conditions of the sea surface height field over sophisticated dynamics and assimilation schemes and leverages the natural propagation direction of ocean height anomalies. It is a computationally economical proof-of-concept tool that provides reasonably accurate sea level forecasts for areas with high risk of inundation. This work forms the basis for developing useful, community-facing tools for stakeholders with interest in coastal communities. The study focuses especially on the islands of Oahu and Hawaii, and in particular on the sites of federally-maintained tide gauges in Honolulu Harbor and Hilo. Oahu was chosen due to its high demand in sea level forecasts for its tourist-driven economy, and Hawaii due to the location of the Hilo tide gauge in the planetary wave regime east of Hawaii Island (see Chapter 2.6.2), which may contribute to the predictability of sea level. There is also ample anecdotal evidence of frequent high-tide flooding in Hilo, suggesting this location can benefit from accurate sea level forecasts.

To produce the observation-based sea level forecasts, we investigated the potential to increase non-tidal sea level predictability for high-profile areas in the Hawaiian Islands by leveraging the natural westward propagation of sea level anomalies in the open ocean. We first investigate the various mechanisms contributing to sea level variability around the Hawaiiian Islands and determine the fractions of variability captured by each process (Chapter 2). We then develop an approach to forecasting sea level anomalies that is computationally economical and primarily relies on observations of sea surface height from satellite altimetry instead of dynamical models (Chapter 3). The satellite altimetry data are used to estimate phase speeds and propagate the large-scale sea level anomalies from east to west towards the Hawaiian Islands using the estimated phase speeds. The skill of hindcasted

anomalies using this approach exceeds the baseline performance of a persistence forecast, suggesting that the methods developed here may have utility in operational coastal management. Finally, we test the ability of the forecasted sea level anomalies to improve forecasts of high-tide flooding frequency on seasonal time scales (Chapter 4). The findings from the study resulted in other study potential around the Hawaiian Islands to increase understanding in generating sea level predictions with a higher skill (Chapter 5).

Chapter 2

Drivers and potential predictability of sea level variability in Hawaii

Sea level variability around the Hawaiian Islands reflects a variety of dynamic processes. The most extreme sea levels are often associated with periods of time when multiple factors contribute to higher sea level simultaneously, producing a stacking effect that has been termed Nu‘a Kai (Figure 2.1; *Yoon et al.*, 2018). Nu‘a Kai is an Hawaiian term meaning “piled ocean” and conveys the sense of multiple components of sea level variability stacking together to produce impacts at the coastline. Primary contributors to sea level around the Hawaiian Islands include long-term sea level rise, astronomical tides, oceanic planetary waves, oceanic mesoscale eddies, and the inverse-barometer effect. The contributors represent diverse scales in both space and time, and each contributor could be a source or barrier of sea level predictability depending on the timescale of interest.

2.1 Long-term sea level rise

Sea level rise due to climate change has contributed to recent high sea levels and high-tide flooding in coastal areas of the Hawaiian Islands. The effect of long-term sea level rise is evident in long tide gauge records around the Hawaiian Islands, but it is important to note that tide gauges record relative sea level change, meaning sea level change relative to a fixed

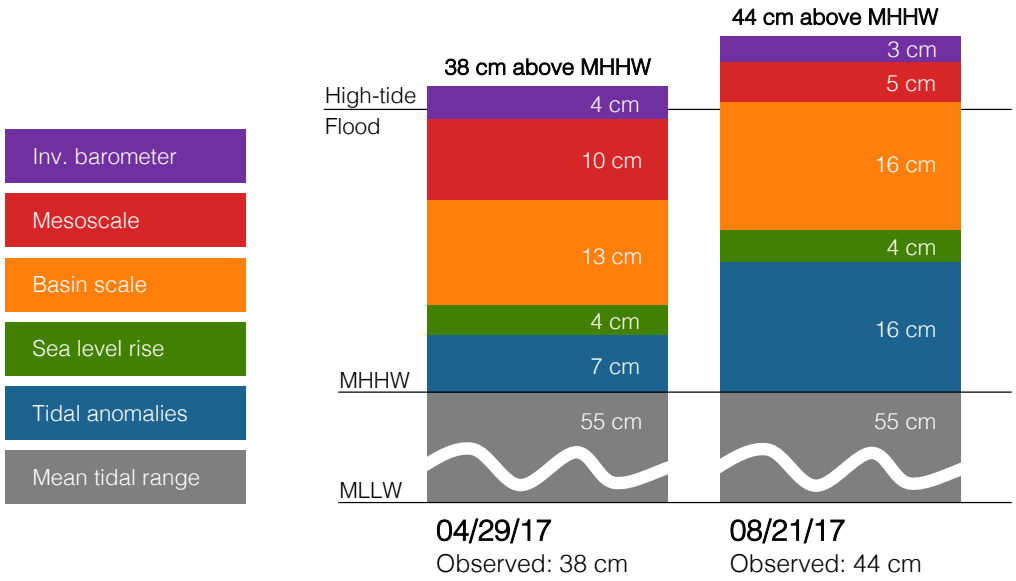

Figure 2.1: The stacking effect of the contributors at the Hawaiian Islands for two high sea level events in 2017 on April 29 (left) and Aug 21 (right). The figure shows that propagating sea level anomalies, such as the large scale and mesoscale anomalies, had a large impact on the total stacking effect.

point on land. Thus, sea level trends from tide gauge data include changes in the absolute level of the ocean related to climate change and oceanographic processes, as well as the effect of vertical land motion. For this reason, long-term sea level trends from tide gauges in Hawaii differ depending on location. Tide gauge data obtained from the National Ocean Service (see Section 3.2.2) show a linear sea level trend in Honolulu, Oahu during 1914–2019 of 1.35 $\pm$ 0.05 mm/yr, while the long-term trend for Hilo, Hawaii during 1946–2019 is 3.05 $\pm$ 0.09 mm/yr. For comparison, the trend in Honolulu during the period overlapping the Hilo record is 1.51 $\pm$ 0.08 mm/yr. The factor-of-two difference between the trend in Honolulu and Hilo is largely due to the fact that Hawaii Island is subsiding at a much faster rate than Oahu. Recent rates of subsidence from long global navigation satellite system (GNSS) records show that the rate of subsidence in Honolulu is near zero (0.4 $\pm$ 0.3 mm/yr during 1997–2018), while the rate of subsidence in Hilo is 1.2 $\pm$ 0.2 mm/yr during 1997–2018 (*Yang*

and Francis, 2019). The remaining difference between the trends at the two sites may be due to interdecadal variations in upper ocean temperature (*Caccamise et al.*, 2005).

For the purposes of this work, which focuses on seasonal forecasting, the contribution of long-term, multidecadal sea level trends to near-term mean sea level variability and high-tide flooding events can be considered highly predictable. Most often, high-tide flooding events are defined by water level relative to the Mean Higher High Water (MHHW) tidal datum defined over the National Tidal Datum Epoch (NTDE), which is 1983–2001. Since the midpoint of the NTDE, the long-term trend in sea level has resulted in approximately 4 cm of sea level rise in Honolulu and approximately 8.5 cm of sea level rise in Hilo. These values can be interpreted as the contribution of sea level rise to present-day high-tide flooding events when defined relative to current tidal datums. The contribution of sea level rise to high-tide flooding in the near future can be predicted by simply extrapolating the multidecadal trend over the forecast period.

2.2 Astronomical tides

Astronomical tides are generated by harmonic gravitational forcing upon the ocean within the Earth-Moon-Sun system. Other planets in the solar system also exert gravitational forces upon the ocean, but the tidal amplitude produced by other planets is too small to observe. Astronomical tides have been extensively studied and observed throughout human history. Due to the harmonic nature of tidal constituents and available long-term sea level time series in Hawaii, the astronomical tides are a highly predictable—approximately deterministic—component of sea level around the Hawaiian Islands (e.g., *Schureman*, 1941; *NOAA*, n.d.c).

The tidal regime in Hawaii is mixed (i.e., not purely diurnal or semidiurnal) with two unequal high tides per day. Tidal ranges are small to moderate around the islands with great diurnal ranges—defined as the difference between Mean Higher High Water (MHHW) and Mean Lower Low Water (MLLW)—of less than one meter. The great diurnal range

defined over the NTDE (1983-2001) is 58 cm for the Honolulu, Oahu tide station, 69 cm for the Kahului, Maui station, and 73 cm for the Hilo, Hawaii station (*NOAA*, n.d.a). It is important to note, however, that the tidal range is not constant in time. Tidal amplitude varies seasonally in Hawaii with astronomical high tides in Honolulu, for example, regularly exceeding 20 cm above MHHW during the summer months of June-August, as well as the late fall and winter months of November-January. The Highest Astronomical Tide (HAT) datum is defined as the highest predicted astronomical tide during the NTDE, which is useful as an estimate of the maximum possible contribution to water level from astronomical forcing. The HAT is 25 cm above MHHW for the Honolulu station, 26 cm above MHHW for the Kahului station, and 27 cm above MHHW for the Hilo station (*NOAA*, n.d.a).

As mentioned earlier (Chapter 1), coastal flooding in the tropical Pacific Islands often occurs when positive sea level anomalies coincide with high tides. The hope of this study is to increase sea level predictability of the non-tidal components of the oceanographic features to use in combination with the tidal predictions to increase predictability of total sea level for the purpose of forecasting periods of enhanced high-tide flooding.

2.3 Oceanic planetary waves

Oceanic planetary waves are large-scale oceanographic features that occur due to latitudinal changes in the planetary vorticity field associated with the rotation and curvature of the earth (*LeBlond and Mysak*, 1981). Atmospheric planetary waves may only have a few wavelengths around the planet, which is where they get their name (*LeBlond and Mysak*, 1981). Oceanic Rossby waves are the class of planetary waves that is most relevant for sea level variability in Hawaii, which, at the latitude of Hawaii, have a minimum period of roughly 3 months corresponding to a minimum wavelength of a few hundred kilometers.

Before the altimetry data from TOPEX/POSEIDON (T/P) were available, the altimeter data were insufficient to detect Rossby waves (*Chelton and Schlax*, 1996). The de-

velopment of T/P significantly increased the availability to study such large oceanographic features. Planetary waves can be generated locally by the wind field due to local downwelling or upwelling (Ekman pumping) that generates freely propagating open-ocean Rossby waves. Alternatively, oceanic Rossby waves can originate from perturbations of the thermocline level at the eastern boundary (e.g., from Kelvin waves propagating along the eastern boundary). Rossby waves originating from local wind forcing and boundary perturbations have been studied as drivers of the low-frequency sea level variability at midlatitudes, where the Hawaiian Islands are found. *Chelton and Schlax* (1996) observed that the energetic sea level near the eastern boundary has a surprisingly weak westward propagation, which is thought to be due to the seasonal wind forcing. *Fu and Qiu* (2002) confirmed by using a 2-layer dynamic model that in the mid-latitudes, the wind-driven planetary waves are more dominant compared to the boundary-driven planetary waves. This does not mean that the boundary-driven planetary waves are insignificant, as when the modeled wind-driven planetary waves were removed, the residual did show evidence of the boundary-driven planetary waves *Fu and Qiu* (2002).

Unfortunately, at the latitude of Hawaii, the application of the 2-layer dynamic model was not successful in recreating the coastal sea level observed by Hawaiian tide gauges with the available wind forcing (*Firing and Merrifield*, 2004). Moreover, *Chelton and Schlax* (1996) noted that there is phase speed variation along the latitude of Hawaii, which is a consequence of the deepening of the thermocline. Such results show that regardless of the demand for coastal sea level forecasts, it is not a simple task to even hindcast sea level, let alone forecast sea level, at the latitude of Hawaii.

Hovmöller plots of sea surface height anomaly were generated from altimetry data at the latitude of the Honolulu Harbor tide gauge (Figure 2.2) to assess propagation of anomalous sea levels around Hawaii during 2017 (see Chapter 1). The Hovmöller plots show features propagating westward towards the Hawaiian Islands producing a continuous sequence of sea level highs and lows. Estimating the propagation speed as the slope of these propagating

features in the Hovmöller plots is close to Chelton's theoretical propagation speed is 6.94 cm/s. The consistency of this propagation speed suggests that sea level anomalies observed to the east of the Hawaiian Islands could be used to predict sea level at Hawaii.

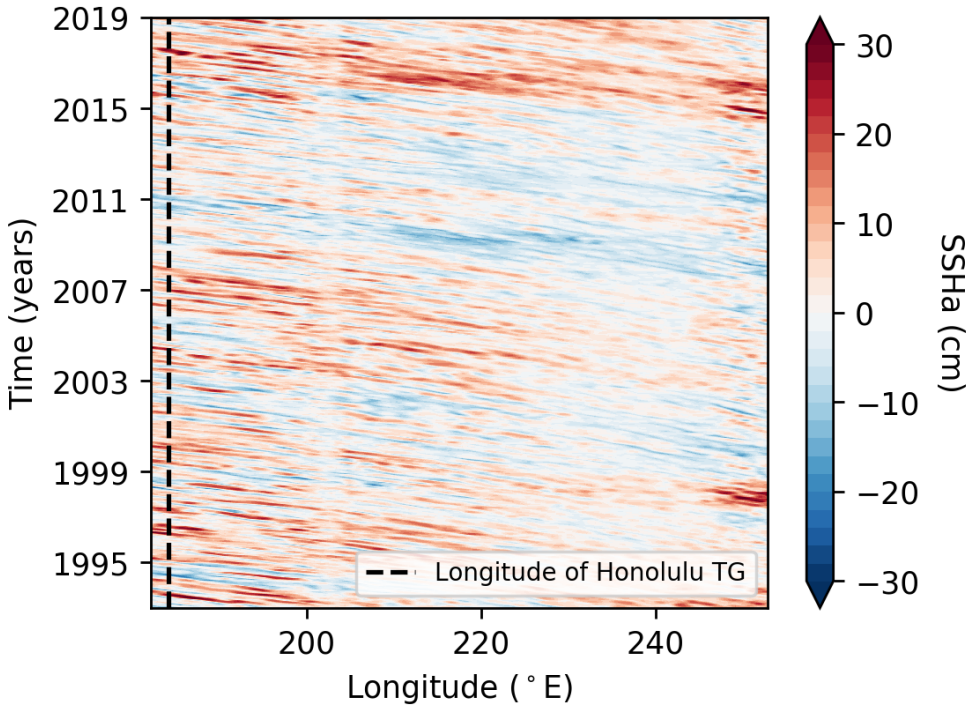

Figure 2.2: Time vs longitude (Hovmöller plot) of CMEMS satellite altimetry observed sea surface height anomalies at the latitude of the Honolulu harbor tide gauge location (21.3°N). The longitude of the Honolulu harbor tide gauge is noted with the black dashed line at (201.1°E).

The long wavelengths, O(1000 km), of these oceanic planetary waves can give the impression that planetary waves propagate in a purely zonal direction. However, *Glazman and Weichman* (2005) showed in their study that there is a significant meridional component to the propagation of planetary waves. There are areas in the ocean where the propagation of the planetary waves are close to purely zonal; however, in mid-latitudes when the periods are shorter than two years, the planetary waves are dispersive in nature and have a meridional component that deviates from zonal propagation towards the equator or the pole by 30° (*Glazman and Weichman*, 2005). Moreover, in Figure 2.2, we see that the sea level anomalies originating from the eastern boundary appear to dissipate within 10° of the boundary. This

is prominently shown in the 1997–98 El Niño, when a large-amplitude sea level high at the coast of Mexico does not propagate across the Pacific Ocean to the Hawaiian Islands, which suggests that most of the zonally propagating sea level anomalies reaching Hawaii are forced by open-ocean Ekman pumping. Assuming that the planetary waves are purely zonal can be an oversimplification; however, as the majority of the energy is known to propagate zonally, this study assumes that the planetary waves are propagating in a purely zonal direction.

2.4 Oceanic mesoscale surface eddies

The oceanic region around the Hawaiian Islands is characterized by complex circulation related to oceanic mesoscale surface eddies. Spatial scales of mesoscale surface eddies vary greatly, though they are typically smaller than 300 km and can persist for months (*Chen and Qiu*, 2010). Oceanic mesoscale surface eddies can be formed due to baroclinic instabilities under the influence of Earth's rotation (*Gill et al.*, 1974; *Wyrtki et al.*, 1976; *Qiu*, 1999). The Coriolis force on the north and south side of the mesoscale surface eddies are different and thus to maintain geostrophic balance, a velocity difference occurs making the eddy drift westward (*Cushman-Roisin and Beckers*, 2011). These mesoscale surface eddies consist of water of their original location and can carry water with varying nutrient content from its current surroundings (*McDonald*, 1999). Cyclonic eddies with cold cores and counterclockwise rotation in the Northern Hemisphere are associated with negative sea surface height anomalies. Anticyclonic eddies with warm cores and clockwise rotation in the Northern Hemisphere are associated with positive sea surface height anomalies (*Cushman-Roisin and Beckers*, 2011).

Mesoscale surface eddies that approach close to the Hawaiian Islands are known to increase or decrease coastal sea level along the archipelago. *Firing and Merrifield* (2004) investigated the extreme high sea level around the Hawaiian Islands that occurred in September 2003. Their findings showed that the anomalous high sea level was generated in large part

due to a mesoscale anticyclonic eddy (i.e., an eddy with clockwise circulation in the Northern Hemisphere) that propagated towards the Hawaiian Islands. These findings are consistent with the sea-level high observed at the Hononlulu tide gauge on April 29, 2017, which is currently the second largest hourly tidal residual anomaly ever recorded at the Honolulu Harbor tide gauge (Figure 1.1). As part of the stacking effect, the anticyclonic eddy that propagated through the Hawaiian Island in April 2017 was a large contributing factor (about 10 cm) to the high sea level event (Figures 2.2 and 2.3, left). The combined effect of the eddy on top of the persisting regional sea-level high related to an oceanic planetary wave and large spring tide made the April 2017 sea level high an even larger event than that of September 2003 studied by *Firing and Merrifield* (2004). Until recently, studies have also not been able to show any clear seasonal pattern for the oceanic mesoscale surface eddies around the Hawaiian Islands; however, *Lindo-Atichati et al.* (2020) found that eddy genesis is higher in spring than fall. The eddies generated during spring and potentially reaching the Hawaiian Islands during the summer months have an amplified effect on coastal sea level due to overlap with the high spring tide events in Hawaii that occur in the summer months.

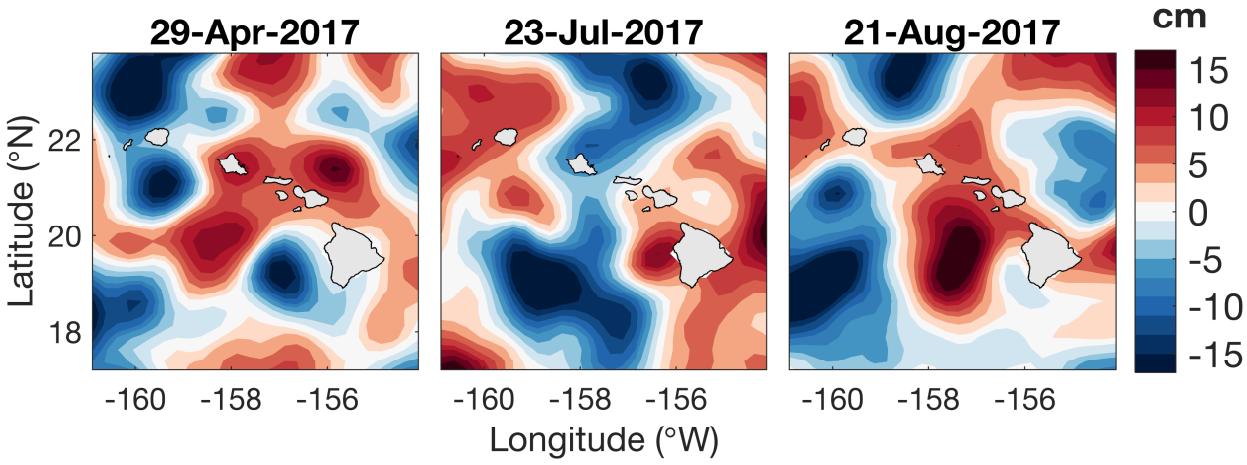

Figure 2.3: Daily mean sea surface height from satellite altimetry (CMEMS) of April 29 (left), July 23 (middle), and August 21 (right) from 2017. The spatial mean has been removed over the spatial domain of each map to highlight mesoscale structures. At all locations, the mesoscale structures are erratic and can increase (right and left) or decrease (middle) the sea level around the Hawaiian Islands.

It is important to note that eddy activity can also mitigate coastal impacts. In summer 2017, July was anticipated to experience the highest sea levels of the year due to coinciding with the highest tides of the year. However, it turned out to be the only month during the April–August period that did not reach the threshold of nuisance flooding (35 cm above MHHW) (Figure 1.1). At the same time as the highest astronomical tide, a cyclonic, cold-core mesoscale eddy approached the Hawaiian Islands producing a negative sea level anomaly (Figure 2.3, middle). Due to the cyclonic mesoscale eddy interfering with the high tides, the sea level in July was high but not to the point that it was exacerbating coastal impacts on beaches and coastal roads. This event underscored the importance of oceanic mesoscale eddies and how tidal predictions are reliable but do not inform of all oceanic features that may greatly affect the sea level.

Oceanic mesoscale eddies are oceanographic features that are difficult to predict, and thus represent a barrier to sea level predictability. Despite a tendency to propagate westward on average, the eddy field can be described as geostrophic turbulence with individual eddies constantly forming, dissipating, merging, and splitting. These eddies, even more so than planetary waves, have trajectories that are not purely zonal with meridional components that are less predictable than the zonal components of propagation. Nevertheless, the methods developed here will attempt to leverage the tendency of mesoscale eddies to propagate in the zonal direction from east to west.

2.5 Inverse-barometer effect

The inverse-barometer effect is the response of sea level to atmospheric barometric pressure systems above the sea surface. The inverse-barometer effect is described by the following equation:

$$\eta_{ib} = -\frac{1}{g\rho_0}(P_{atm} - P_0) \tag{2.1}$$

where η_{ib} is the local sea level adjustment due to the atmospheric pressure, g is the gravitational constant, ρ_0 is the seawater density, P_{atm} is the atmospheric pressure, and P_0 is a reference atmospheric pressure. The sea level and the atmospheric pressure are inversely proportional and, in general, it could be simplified as a linear relationship where a 1 mbar increase in atmospheric pressure leads to a sea level decrease of 1 cm. A high-pressure system will cause sea level to fall, and a low-pressure system will raise the sea level. Around the Hawaiian Islands, the atmospheric pressure can range from 1000 – 1027 Pa and is typically 1016–1017 Pa. The relation between the sea level and the atmospheric pressure is straightforward and well measured. However, the predictability of the inverse-barometer effect is heavily reliant on the predictability of atmospheric pressure forecasts, which are essentially weather forecasts. As we can only reliably predict weather a few days in advance, the inverse-barometer effect of atmospheric pressure on the ocean has extremely low predictability at seasonal time scales. The contribution may be great depending on if there is a low atmospheric pressure system at the point of interest; therefore, there is a potential that the inverse-barometer effect would be a barrier in predictability. At the island of Oahu, the largest impact from the inverse-barometer effect since the mid 20th century as been about 10 cm. However, this was an isolated anomaly, and data shows that the contribution of the inverse-barometer effect to sea level exceeds 4 cm (i.e., above the effect of the long-term sea level rise) just 5 percent of the time. Therefore, its general effect is small, and despite its lack of predictability, the inverted barometer effect does not present a significant barrier to predicting the majority of sea level variability in Hawaii.

2.6 Regimes of sea surface height variability around the Hawaiian Islands

The main Hawaiian Islands are a relatively small archipelago in the middle of the Pacific Ocean, but sea level variability around the islands shows that these islands spanning merely

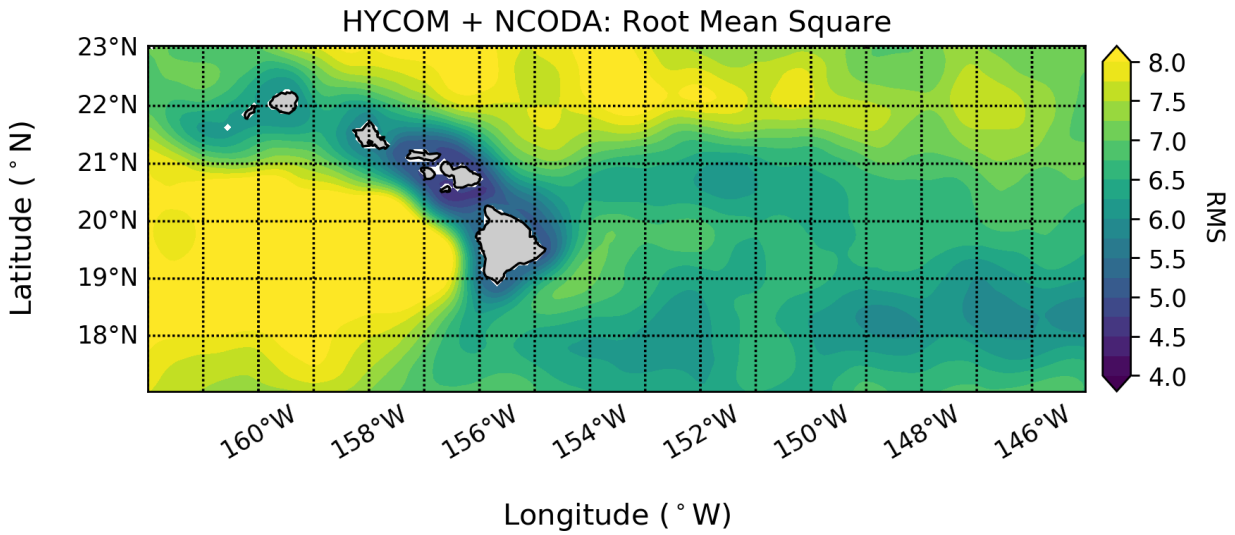

Figure 2.4: The root mean square of the sea surface height (cm) around the Hawaiian Islands from HYCOM+NCODA showing sea level variability around the islands. The yellow regions showing the eddy dominant region (west of the islands and north east of the islands), the dark blue around the contours of the islands showing areas of low sea level variability, and the green areas showing the Rossby dominant regions (south of 21°N).

3 degrees of latitude reside in a complex oceanographic region with multiple dynamical regimes. To demonstrate these regimes, a map of the root-mean-square (RMS) of sea surface height variability (Figure 2.4) is created using the $1/12° \times 1/12°$ gridded sea surface height data from the HYbrid Coordinate Ocean Model (HYCOM) and the Navy Coupled Ocean Data Assimilation (NCODA) (HYCOM+NCODA). The model output is used in this case instead of the gridded alimtery observations, because the gridded altimetry product smooths the height observations across the Hawaiian Ridge, which is known to be an important oceanographic boundary. The HYCOM+NCODA model does, however, assimilate available satellite altimeter observations along the satellite tracks. The RMS map from HYCOM+NCODA highlights four regimes around the Hawaiian Island that show different oceanic features dominating the area. The four regimes, which will be described below, are (1) an oceanic mesoscale-eddy-dominated region to the west of the islands, (2) a comparatively quiescent region to the southeast of the islands that is likely dominated by oceanic planetary waves, (3) a region of low variability following the topography of the island chain,

and (4) a region to the northeast of the islands influenced by a combination of mesoscale eddies and planetary waves.

2.6.1 Wind-generated mesoscale eddies

Oceanic mesoscale eddies are prevalent around the Hawaiian Islands due to complex flow and atmospheric variability. The region of high RMS to the west of the Hawaiian Islands (Figure 2.4) is dominated by mesoscale eddy variability related to prevailing northeasterly trade winds and island topography (*Lumpkin and Flament*, 2001; *Yoshida et al.*, 2010). These eddies are generated by differential surface wind stress in the lee of the islands that produces localized Ekman pumping and eddy formation. The eddies formed in this region tend to propagate westward and away from the Hawaiian Islands, but they can also propagate northwest along the ridge and impact coastal sea level of the islands along the way.

2.6.2 Oceanic planetary waves

To the east of the Hawaiian Islands and at latitudes lower than 21°N is a region of comparatively low RMS suggesting reduced eddy variability and potentially indicating increased influence of oceanic planetary waves on the surface height field (Figure 2.4). Here, there are large-scale sea surface anomalies persistently propagating towards the Hawaiian Islands. Hawaii Island is directly west of this region, which makes Hawaii Island a promising candidate for high predictability from observation-based sea level forecasts.

2.6.3 Reduced variability following topography

Directly around the Hawaiian Islands following the topographic contours, there is a region of low surface height variability surrounding the islands. This low variability is present in both the sea surface height model and in altimetry data (not shown) and is seen as a dark blue region in Figure 2.4. The RMS of tide gauge data is consistent with reduced variability near

the islands. The RMS values of daily mean tide gauge data from Hilo Harbor, Honolulu Harbor, and Kahului are 5.23, 4.70, and 4.40 cm respectively. The reason for this low variability near the topography is not completely clear. To some extent, one might expect open-ocean eddies to be unable to approach close to the coastlines of Hawaii due to the interaction of the ridge topography with the deep signatures of the eddies, which can reach hundreds or even a thousand meters depth. On the contrary, *Firing and Merrifield* (2004) and *Yoon et al.* (2018) document the influence of mesocale anomalies on high sea level events. The extent to which the topography of the ridge damps coastal sea level variability associated with the open-ocean mesoscale eddies and the conditions under which eddies do, in fact, influence coastal sea level are important questions for future investigation. The ability to project the influence of open-ocean sea level anomalies onto coastal sea level would be an important contribution to improving coastal sea level forecasts in Hawaii. For this study, the reason for reduced sea surface height variability around the topographic contours will be left for future work.

2.6.4 Instability-generated mesoscale eddies

The fourth and final regime of sea surface height variability around the Hawaiian Islands is the region of combined mesoscale eddy and oceanic planetary waves to the east of the Hawaiian Islands and north of 21°N (Figure 2.4). This region shows high RMS values (though not as high as the region to the west of the islands) suggesting enhanced eddy activity relative to the region to the south. The mesoscale eddies here are locally generated due to instability associated with the vertically sheared North Equatorial Current (*Chen and Qiu*, 2010). The region is east of Oahu, and eddies generated in this region would tend to propagate to the west and potentially impact Honolulu sea level, which is a location of prime interest.

2.7 Coastal vs. open ocean sea level

For this study, the focus is on using open-ocean propagating sea level anomalies to forecast coastal sea level. In Chapter 2.6.3, it was shown that along the topographic contours of the Hawaiian Islands resides a different kind of sea level regime exhibiting reduced variability in sea surface height compared to the open ocean. Is the region of low sea level variability in coastal areas an artifact of the altimetry and the model? If not, is the coastal sea level sufficiently coherent with the open-ocean sea level to justify using open-ocean sea level in an observation-based coastal sea level forecast?

The spectral coherence of tide gauge inverted-barometer-corrected sea levels between the gauges at Honolulu (Oahu), Kahului (Maui), and Hilo (Hawaii) show the degree of coherence of coastal sea level across the island chain (Figure 2.5) and within the regime of reduced sea level variability following the topography (Section 2.6.3). Honolulu and Kahului sea levels are highly coherent (Figure 2.5B) and in phase (Figure 2.5D) at low frequencies, including the monthly to seasonal time scales of interest in this work. In contrast, sea levels from the gauge at Hilo are not coherent with either of the other two locations (Figure 2.5B), even at the lowest frequencies, which suggests that a single seasonal sea level forecast for all of Hawaii is not sufficient. There are substantial differences in sea level even within the region of reduced variability following topography. Similar conclusions can be made from examining the coherence of the closest grid points to each tide gauge from the gridded altimetry data (Figure 2.6). There is high coherence in the open-ocean sea level between Honolulu and Kahului for periods longer than 30 days, but little coherence in the open-ocean sea level between Hilo and the other locations (Figure 2.6B). The result is consistent with the fact that Honolulu and Kahului reside in the regime where both eddy and planetary waves are important, while Hilo resides in a region of comparatively low eddy activity likely dominated by oceanic planetary waves (Chapter 2.6). This further underscores the need for distinct forecasts for different locations in Hawaii.

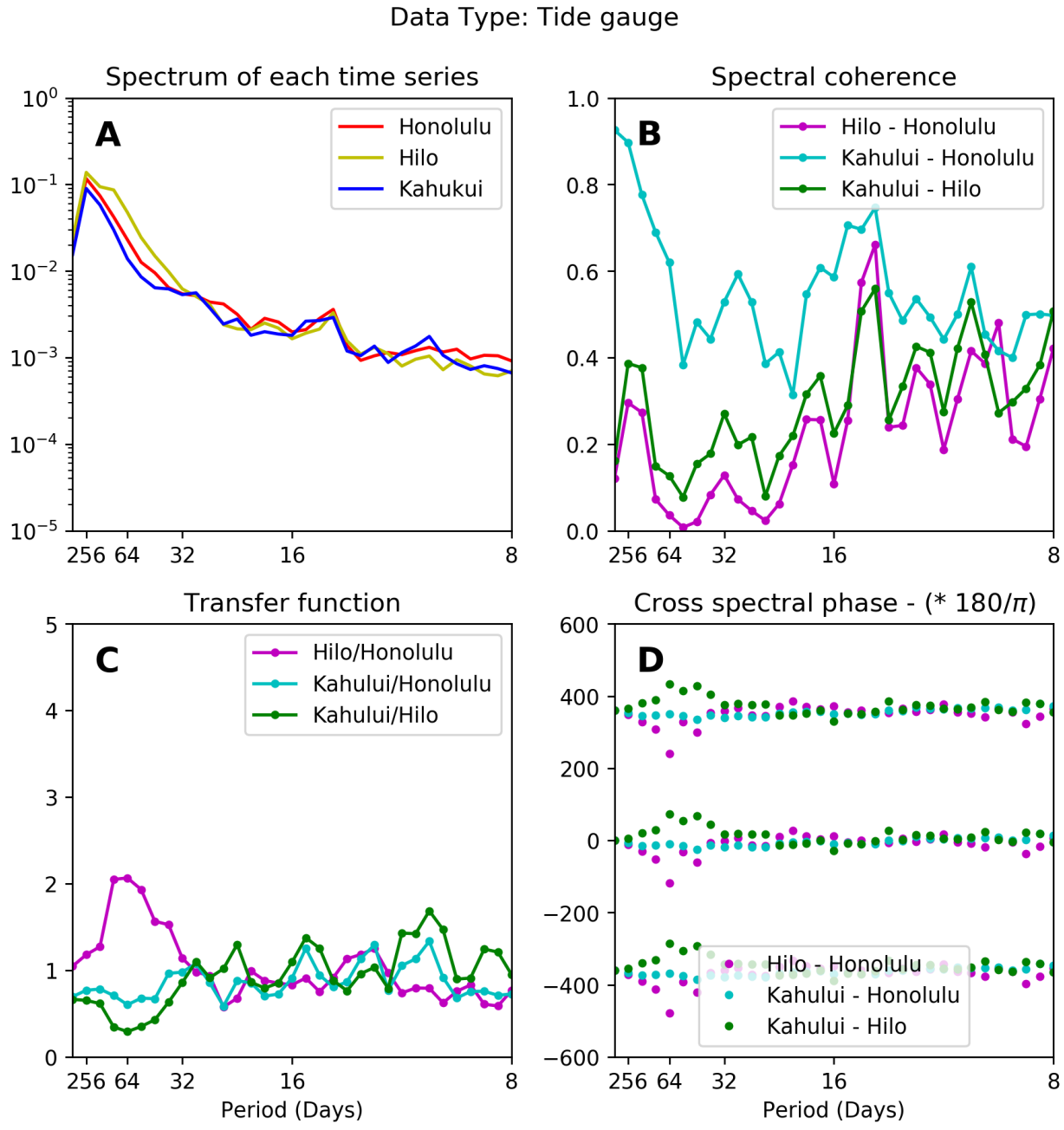

Figure 2.5: Spectral analysis of observed TG sea level between three TG locations around the Hawaiian Islands (Hilo, Honolulu Harbor, and Kahului) showing (A) individual spectrum, (B) spectral coherence, (C) transfer function, and (D) cross spectral phase. The spectral coherence shows that there is coherence between the Kahului and Honolulu Harbor (cyan) observed TG sea level. For Hilo, the spectral coherence is present for both Kahului (green) and Honolulu Harbor (purple) for higher frequencies.

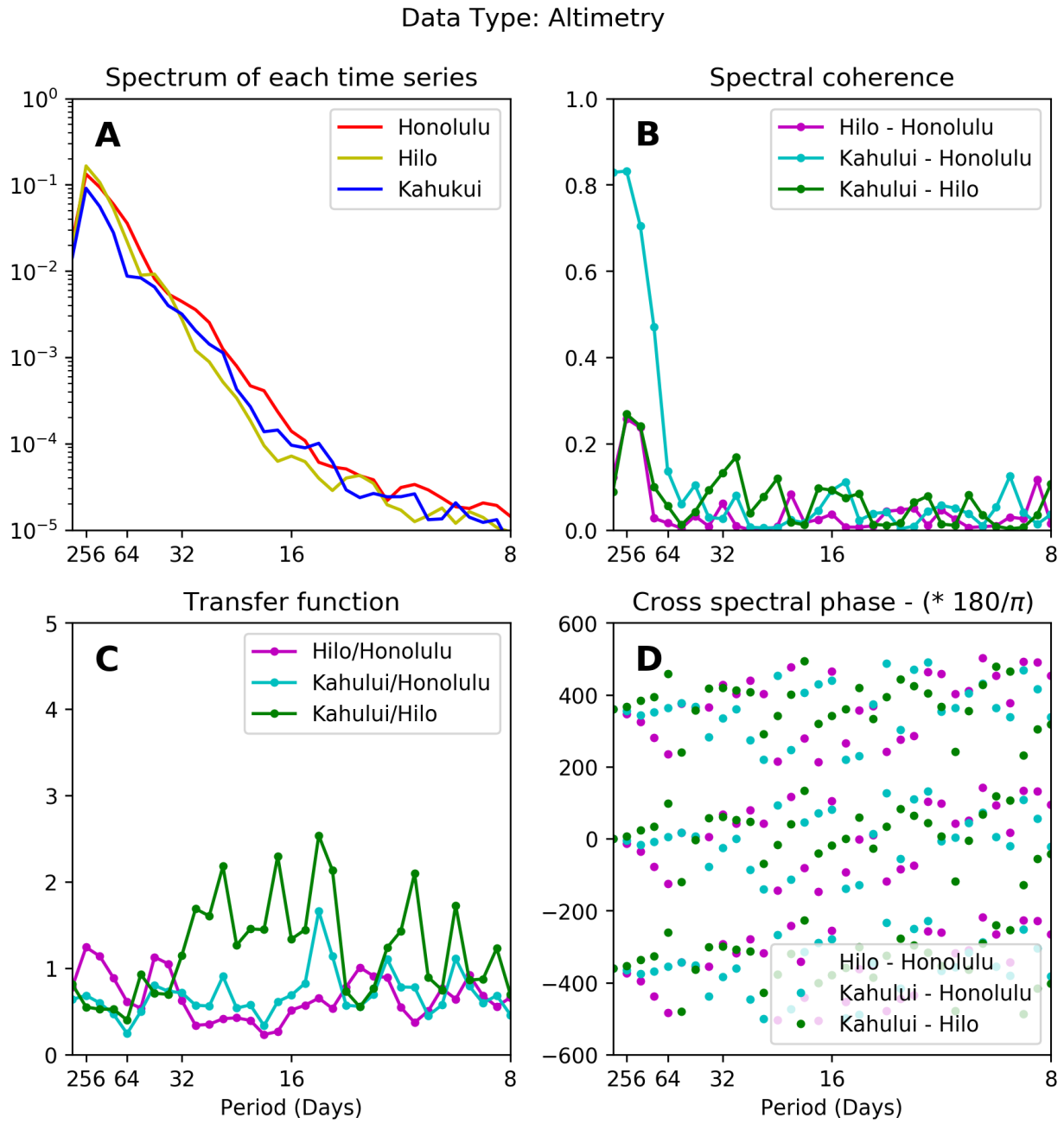

Figure 2.6: The spectral analysis of open ocean sea level between three CMEMS altimetry sea surface height anomalies grid points around the Hawaiian Islands closest to the Hilo, Honolulu Harbor, and Kahului TG locations showing (A) individual spectrum, (B) spectral coherence, (C) transfer function, and (D) cross spectral phase.

The coherence analyses above demonstrate the degree of coherence between different locations and data of the same type (i.e., tide gauge to tide gauge or altimetry to altimetry), but what about coastal (tide gauge) vs. open-ocean (altimetry or model) data at the same location? By conducting spectral analysis between coastal and altimetry open ocean sea level at Honolulu, Kahului, and Hilo we found that there is a high degree of spectral coherence between open-ocean and coastal sea level for periods longer than 30 days, but there is little to no spectral coherence for periods shorter than 30 days (Figure 2.7). This is not only true for the altimetry, but also true for the HYCOM+NCODA model. This is important, because it was suspected that the drop in spectral coherence for periods shorter than 30 days for altimetry may be due to the gridding algorithm of the altimetry to data to combine height data from both sides of the Hawaiian ridge. The fact that a similar drop in coherence occurs in the model, whic assimilates along-track altimetry data and has much higher resolution, suggests this is not the case.

A time series analysis was also conducted to confirm the results from the spectral analysis. The time series from the pressure corrected tide gauge and altimetry sea level data were correlated together in three forms: (1) no temporal split, (2) low-pass filtered at 30 days, and (3) periods shorter than 30 days, i.e., residuals from the low-pass filter (Figure 2.8). The correlation for both Hilo and Honolulu were the highest when the sea level was low-pass filtered at 30-days, with very little correlation for sea level periods shorter than 30 days. The correlation between the tide gauge and the altimetry data confirm the results from the spectral coherence, that to use open ocean data from satellite altimetry for the proposed observation-based sea level forecast, we would apply a 30-day low-pass filter on the altimetry data to reflect the periods that are most reflective of the coastal sea level at the Hawaiian Islands.

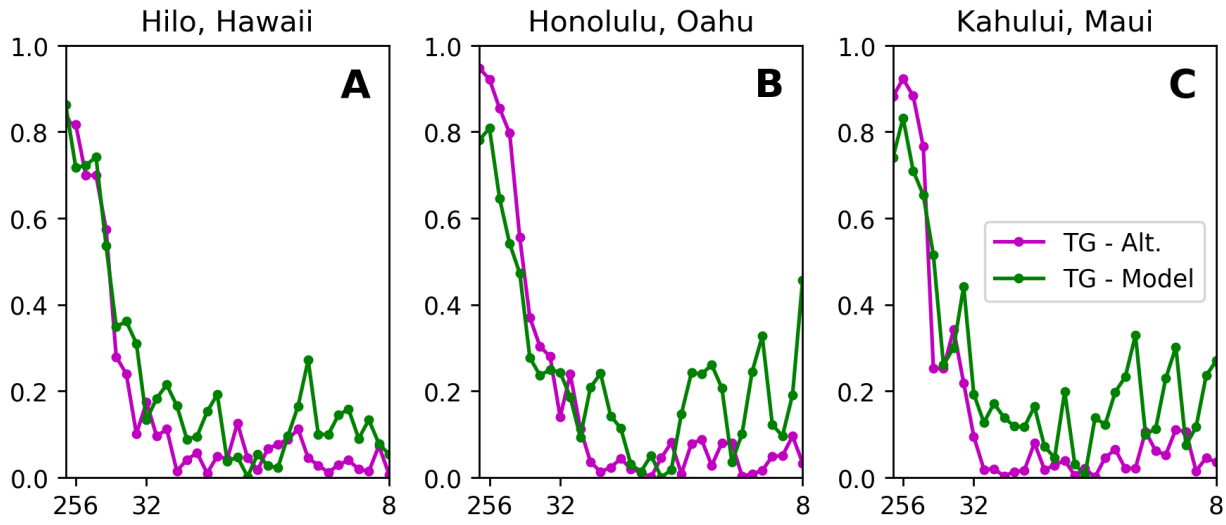

Figure 2.7: The spectral coherence of observed TG coastal sea level and open ocean sea level (CMEMS altimetry and HYCOM+NCODA sea surface height anomalies) grid points closest to the TG locations for Hilo (A), Honolulu Harbor (B), and Kahului (C). The spectral coherence at all locations show that there is coherence between coastal and open ocean sea level for periods longer than 30 days. HYCOM+NCODA sea surface height anomalies were used to see if the higher resolution models results different due to its better representation of island geometry, but the results are consistent with the CMEMS altimetry results.

	Hilo	Honolulu
Detrended daily tide gauge sea level variance	36.91	28.34
Inverted barometer effect	5.23 (14)	7.01 (25)
Low-frequency, large-scale (periods >30 days, scales >300 km)	16.72 (45)	12.10 (43)
Low-frequency, mesoscale (periods >30 days, scales <300 km)	3.46 (9)	4.58 (16)
Residual (periods <30 days, non-inverted barometer)	12.01 (33)	7.73 (27)

Table 2.1: Components of daily sea level variance in cm^2 during the altimeter era, 1993–2018. The percentage of overall detrended sea level variance is given in parentheses.

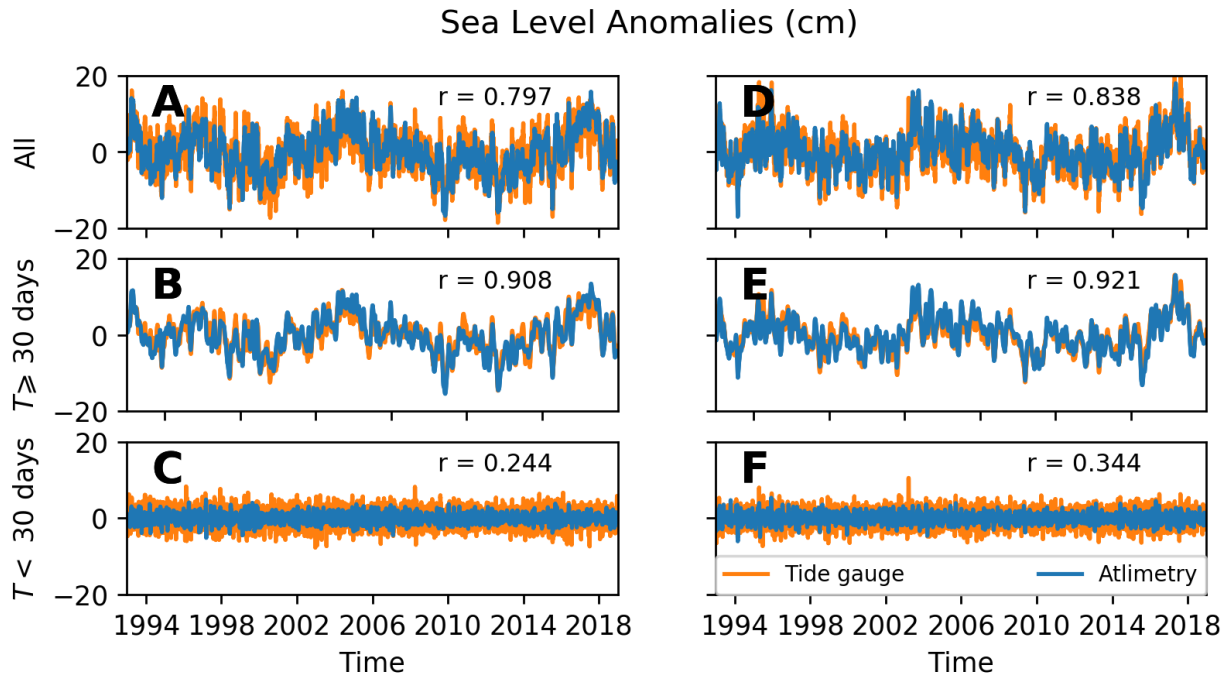

Figure 2.8: Time series and correlations of IB corrected tide gauge sea level (orange) and CMEMS altimetry sea level (blue) at Hilo (left) and Honolulu (right). The top panel shows the sea level without any temporal smoothing, and the correlation between the TG and altimetry are high for both Hilo and Honolulu, 0.80 and 0.84 respectively. The middle panel shows the sea level where a 30-day low pass filter has been applied to both TG and altimetry, and the correlation increased to 0.91 and 0.92 at Hilo and Honolulu, indicating the open ocean sea level can be representative of coastal sea level for periods longer than 30 days. The bottom panel shows the high frequency (periods shorter than 30 days) sea level and the correlation between the TG and altimetry drops drastically to 0.24 and 0.34 for Hilo and Honolulu.

2.8 Importance of low-frequency sea level variability

After identifying the time scales and processes that may contribute to predictability of sea level in the Hawaiian Islands, an assessment was made to see what fraction of the daily mean sea level variability might be predictable. To assess this, the overall daily sea level variance and the variance of the relevant components were calculated for the Honolulu and Hilo tide gauge records during the period overlapping the altimetry era (Table 2.1). The procedures for separating the various components of the daily sea level variance are described in detail in Chapter 3.3. The Hilo sea level data has on overall greater variance than the Honolulu location, which is surprising given the proximity of Honolulu to the regions of greater open-ocean variability compared to Hilo (Figure 2.4). The inverted barometer effect, calculated from atmospheric pressure data, accounts for a substantial fraction—roughly a quarter at Honolulu—of the detrended daily sea level variance. As stated earlier in this chapter, this fraction of the sea level variability is not likely to be predictable. The low-frequency, large-scale and low-frequency mesoscale components are calculated by applying a 30-day low-pass filter to the altimetry data and then applying a 300 km Gaussian spatial filter to separate the mesoscale from the large-scale. The low-frequency, large-scale variability—the component most likely to exhibit a high degree of predictability—accounts for approximately 45% of the detrended daily sea level variability at both locations. Combining the low-frequency, large-scale variability with the low-frequency, mesoscale—which may contain some element of predictability—gives 50–60% of the detrended daily sea level variability that can be assumed to have a westward-propagating component to be leveraged for observation-based sea level forecasts.

Despite large fractions of the detrended daily sea level variance not falling into a predictable category of variability, there is still significant utility in generating low-frequency seasonal mean sea level forecasts. The utility comes from the fact that the low-frequency variations change the baseline about which higher-frequency sea level variations occur, which

is important for identifying periods of time when the frequency of high-tide flooding will be increased. When viewed against the backdrop of hourly sea level variability (including tidal cycles) the low-frequency (30 days and longer) sea level is a small fraction of the overall sea level variance, and the long-period variability is not large enough to exceed the high tide flooding threshold by itself (Figure 2.9, black dotted line). However, these low-frequency variations can make the difference between a given month experiencing zero or many threshold exceedances depending on the height of the threshold (Figure 2.9). To demonstrate the utility of forecasting sea level at periods longer than 30 days, the number of days per month with at least one hour exceeding an arbitrary threshold of 25 cm above MHHW are plotted against two predictors (Figure 2.10). The first is the 99th percentile of tidal variability in each month, which captures the effect of seasonal to decadal changes in tidal amplitude. The relationship of monthly exceedances to this predictor is weak, because it does not capture the impact of mean sea level variations on the baseline around which tides oscillate (Figure 2.10, left). In contrast, if we add the first predictor to monthly mean sea level, the relationship between the predictor and threshold exceedances is greatly improved (Figure 2.10, right). Thus, sea level forecasts of monthly and longer periods leveraging the propagating anomalies at large and mesoscales can potentially improve preparedness for periods of enhanced high-tide flooding in Hawaii.

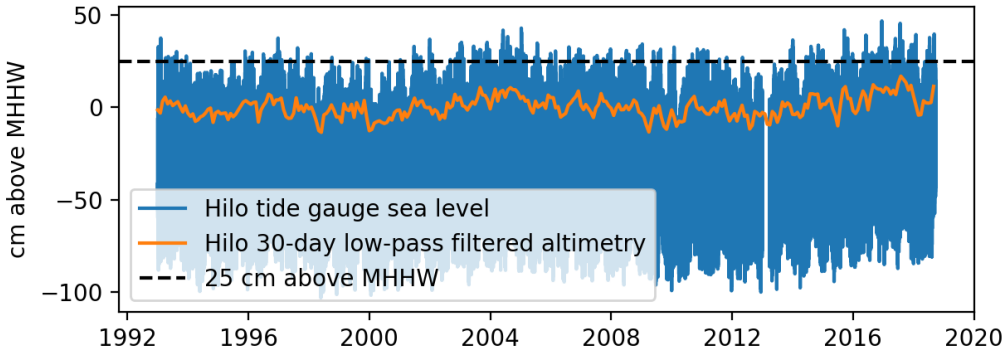

Figure 2.9: Hourly TG sea levels (blue) and daily 30-day low pass filtered CMEMS altimetry sea level (orange) for Hilo, Hawaii. For reference, the 25 cm water level is shown (dashed horizontal line), which is a threshold for coastal impacts near Hilo. 30-day and longer periods make up a small fraction of overall hourly sea level variance.

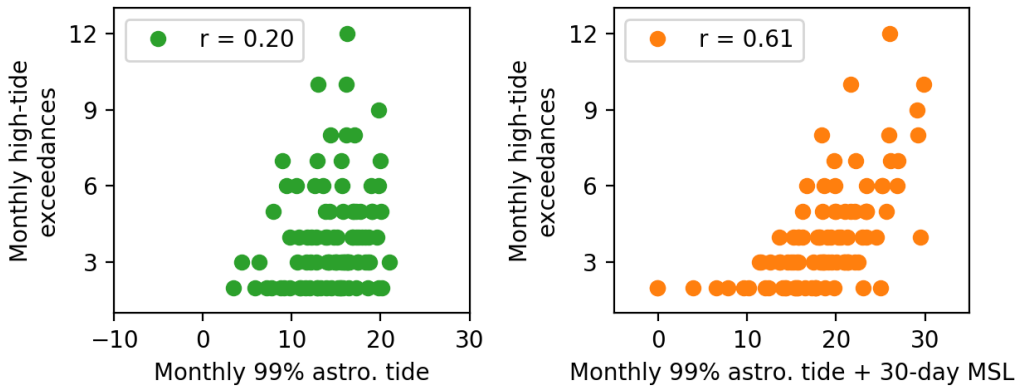

Figure 2.10: Predictors of monthly high tide threshold exceedances calculated with tide predictions (left) and with both tide predictions and 30-day low-pass filtered mean sea level (right) for Hilo, Hawaii. Regardless of periods longer than 30-day and longer make up a small fraction of overall hourly sea level variance (Figure 2.9), the predictors of monthly high tide threshold exceedances that include long-period mean sea level variation are more skillful (right).

Chapter 3

Observation-based forecasts of coastal sea level in Hawaii

3.1 Overview

The overarching premise of the forecasting methodology developed here is that sea level anomalies to the east of the Hawaiian Islands will tend to propagate westward and alter coastal sea level of the islands at some later time determined by the speed of propagation. Analysis of tide gauge and altimetry data demonstrated that coastal sea level in Hawaii measured by tide gauges is related to open-ocean sea level at periods longer than 30 days (Chapter 2.7). Thus, the methodology developed here will focus on forecasting sea level anomalies at periods longer than 30 days. Results from previous studies in the literature and analysis of sea surface height variance around the island chain suggest that coastal sea level from different locations along the archipelago are not equally impacted by mesoscale and large-scale open-ocean anomalies (Chapter 2.8). For this reason, the effects of these different spatial scales are separated in the observation-based forecasts, and the relative skill of each spatial scale in the forecasts is independently assessed.

The observation-based forecast procedure can be outlined as follows. More detail on the datasets, data processing, and training/validation methodology follows in subsequent sections.

1. Pressure correct the tide-gauge observations (Chapter 3.3.1).
2. Detrend, deseason, and low-pass filter the tide-gauge and altimetry observations (Chapters 3.3.2 and 3.3.3).
3. Apply a spatial filter to the altimetry data to separate mesoscale and large-scale variability (Chapter 3.3.4).
4. Perform a lag-correlation analysis between the tide-gauge data and altimetry data to the east of the islands.
5. This is performed independently for the mesoscale and large-scale variability (Chapter 3.4.2).
6. Use the lag-correlation analysis to establish a zonal propagation speed for the mesoscale and large-scale components of the variability (Chapter 3.4.2).
7. Create naïve forecasts for the mesoscale and large-scale components by zonally propagating observed anomalies for each scale at the calculated speeds (Chapter 3.4.3).
8. Create a persistence forecast by assuming the tide gauge sea level anomalies persist indefinitely (Chapter 3.4.1).
9. Regress observed tide-gauge anomalies onto the persistence forecast from the tide gauge and naïve mesoscale and large-scale forecasts from altimetry (Chapter 3.4.4).
10. Construct the observation-based forecast based on the optimal combination of these three components resulting from the regression (Chapter 3.4.4).

Preliminary analyses suggest two hypotheses to test using the forecast framework:

- **Hypothesis 1:** Variability with larger spatial scales will exhibit greater predictability due to its tendency to be more coherent in time and greater tendency to propagate zonally for greater distances. Conversely, variability with shorter spatial scales will be less predictable due to its tendency to exhibit more chaotic and less purely zonal motion.
- **Hypothesis 2:** Honolulu coastal sea level will be less predictable compared to Hilo due to the proximity of Oahu to the eddy-rich regions to the west and northeast of

the archipelago. In contrast, Hilo is situated adjacent to the comparatively quiescent region, in terms of SSH variability, to the east of Hawaii Island.

3.2 Data

3.2.1 Satellite altimetry

For this study, the satellite altimetry data used are from Copernicus Marine Environment Monitoring Service (CMEMS; formerly AVISO). The CMEMS daily altimetry gridded data are a multimission altimeter product, where the data from all altimeter missions (Saral, Cryosat-2, Jason-1 and -2, T/P, Envisat, GFO, ERS-1 and -2, and Geosat) are processed to generate a single dataset. The CMEMS gridded data used in this study are the sea level anomalies (MSLA): Height (H) (MSLA-H), which uses a 27-year mean sea level height to compute the anomalies. The resolution of the CMEMS gridded data are $1/4^\circ \times 1/4^\circ$. CMEMS provides both delayed time altimetry data (currently available between January 1st, 1993 to March 7th, 2020) and the daily near-real-time data uploaded once a day to the present day. The publication of the daily near real-time data will allow the observation-based sea level forecast to generate sea level projections in near real-time. Corrections are made for ocean response to wind and pressure forcing and the inverse barometric effect in the distributed MSLA-H; this theoretically eliminates the atmospheric variation from the CMEMS MSLA-H data.

3.2.2 Tide-gauge sea level

Tide gauges are instruments that measure relative coastal sea level, meaning sea level relative to a fixed point on land. In this study, we used tide gauges maintained by the National Oceanic and Atmospheric Administration (NOAA). In this study, we specifically used stations 1612340 and 1617760, which are located in Honolulu Harbor (Oahu) and Hilo Harbor

(Hawaii), respectively. Hourly water level data through 2019 and NOAA tidal predictions during the span of each record were obtained directly from the NOAA CO-OPS API (*NOAA*, n.d.b). The first available Honolulu sea level data from the Center for Operational Oceanographic Products and Services (CO-OPS) Application Programming Interface (API) are from 1914, making this tide gauge record one of the longest and highest-quality available. The tide gauge record from Hilo spans 1946 to present. Measurements at the NOAA-maintained tide gauges are recorded every six minutes; hourly averaged data are downloaded for use in this study.

3.2.3 Atmospheric pressure

MSLA-H data from CMEMS has been corrected for the inverse-barometer effect however, the sea level data from the tide gauge are not corrected for similar atmospheric variations. For this reason, sea surface atmospheric pressure data was used to pressure correct the tide gauge data for inverse-barometer effects to ensure fair comparisons between the sea level data from the tide gauges and altimetry. The pressure data used in this study are the daily gridded sea level pressure data from NOAA's National Centers for Environmental Prediction-Department of Energy (NCEP-DOE) Atmospheric Model Intercomparison Project (AMIP)-II Reanalysis (NCEP2) data. The NCEP2 sea level pressure data used to pressure correct the sea surface height data was obtained from the Asia-Pacific Data-Research Center (*APDRC*, n.d.). The data are available in units of pascals (Pa) and currently available from January 1st, 1979 to January 31, 2020.

3.3 Data processing

3.3.1 Pressure correction

As the MSLA-H data from CMEMS has been corrected for the inverse-barometer effect, and the tide gauge-driven sea level height data are not, the sea level pressure data from NCEP2 are used to pressure-correct the sea level data derived from the tide gauges. First, the grid point that is closest to the tide gauge locations is extracted from the NCEP2 sea level pressure gridded-data. As mentioned earlier in Chapter 2.5, the inverse-barometer effect can be approximated to high-accuracy as a linear relationship where an increase of 1 mbar causes sea level to drop 1 cm. In order to utilize this relationship, the pressure data from NCEP2 are converted from Pa to mbars prior to making the inverted-barometer correction.

3.3.2 Trend and seasonal cycle

To focus on the sea level anomalies unrelated to seasonal cycles or long-term sea level rise trends, the sea level height data are detrended and the seasonal cycle is removed from the sea level height data. Seasonal changes in the sea level height are cyclical and predictable, and removing seasonal harmonics will increase clarity in sea level height related to propagating anomalies. The mean sea level and linear trend are also removed to generate a data set that only consists of the sea level height anomalies. The seasonal cycle and trend are calculated by fitting annual and semiannual harmonics simultaneously with a mean and linear trend in a multiple linear regression obtained via least-squares solution to a linear matrix equation. The fitted annual and semiannual cycles, mean, and linear trend are then removed from the sea level data. Detrending and removal of the seasonal cycle are applied to all altimetry data around the Hawaiian Islands, as well as the tide gauge data when direct comparisons are made.

3.3.3 Temporal filter

As mentioned in Chapter 2.7, there is little to no spectral coherence between coastal sea level measured by tide gauges and open-ocean sea level measured by altimeters at periods shorter than 30 days (Figure 2.7). Therefore, a Butterworth temporal low-pass filter with a cutoff period of 30 days is applied to the altimetry data to isolate the open-ocean variability that are most reflective of the coastal sea level at the Hawaiian Islands. Prior to performing the retrospective forecast calculations and evaluating skill, the low-pass filter is applied to both the altimetry data and the tide gauge sea level data to assess the skill of the sea level forecast on the same timescales (Figure 3.1). We do not explicitly treat variability with periods shorter than 30 days in this analysis.

3.3.4 Spatial filter

A 2-dimensional Gaussian filter with a half-width of 300 km is applied to the altimetry sea level data, smoothing in both longitude and latitude. To isolate mesoscale and large-scale variability, the smoothed sea level data are subtracted from the original altimetry sea level data. For example, Figure 3.1 shows two maps of daily sea surface height data from altimetry, and Figure 3.2 shows when the two spatial scales have been separated by the Gaussian filter. Note that the data for each spatial scale are not completely independent, as large-amplitude eddies—such as the ones east of Hawaii Island on July 23, 2017 and west of Hawaii Island on August 21, 2017—have signatures in the maps for both spatial scales (Figure 3.2). In general, the smoothed large-scale sea level data tends to capture the effect of oceanic planetary waves, as well as the broad signature of large-amplitude, spatially-coherent ocean eddies (Figure 3.2, bottom). The mesoscale sea level variability primarily captures the signature of the comparatively weaker and smaller-scale background eddy field around the Hawaiian Islands (Figure 3.2, top).

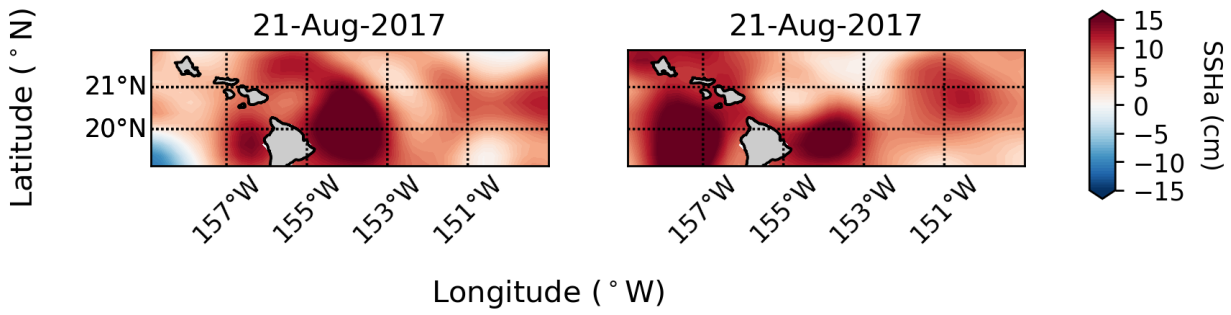

Figure 3.1: 30-day low pass smoothed CMEMS satellite altimetry sea surface height anomaly on July 23, 2017 (left) and August 21, 2017 (right).

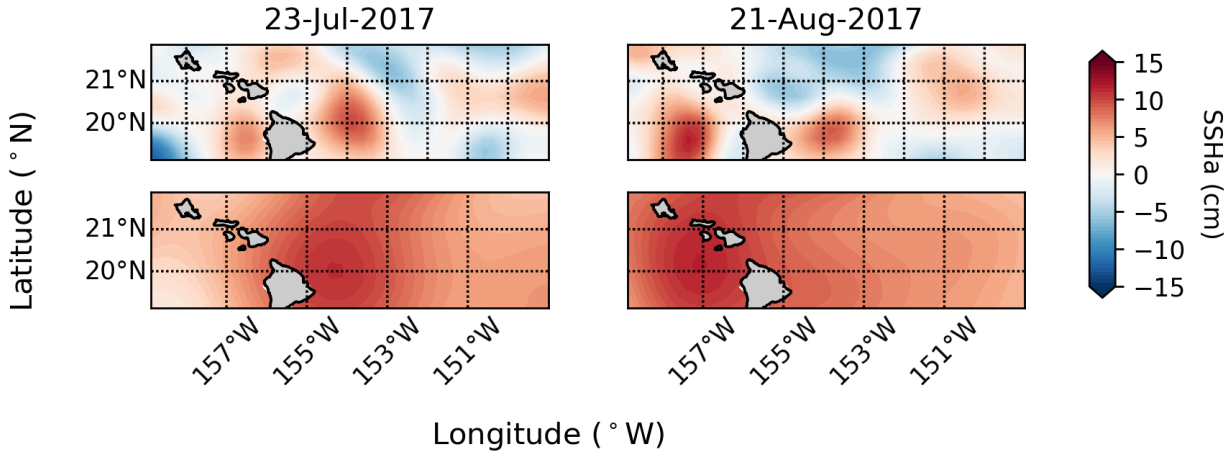

Figure 3.2: 30-day low pass smoothed CMEMS satellite altimetry sea surface height anomaly with a 300 km Gaussian spatial filter applied to separate mesoscale (top) and large scale (bottom) anomalies on July 23, 2017 (left) and August 21, 2017 (right). The 300 km Gaussian spatial filter does not isolate the sea level anomalies clearly, indicating that the two spatial scales are dependent on each other.

3.4 Sea level forecasts

In this section, we will compare sea level persistence forecasts to an optimized observation-based sea level forecast calculated as a weighted combination of persistence and propagation-based sea level forecasts. The propagation-based sea level forecasts are separated into mesoscale and large scale, which are then used in combination with the persistence forecast. The weights for each component of the observation-based forecast are generated via multiple linear regression of tide gauge observations onto the forecast components.

3.4.1 Persistence forecast

Persistence forecasts assume that the sea surface height of today will remain unchanged in the future. Such persistence forecasts are often used to establish a baseline in performance for other more sophisticated forecasts. "Beating persistence" is often the threshold for which a given forecast method can be said to have meaningful skill. In this case, the persistence forecast is generated using data from the NOAA-maintained tide gauges, which are detrended, deseasoned, and low-pass filtered as described in Chapter 3.3 above. Note that the inverted barometer correction is applied. For any given forecast period, the persistence forecast is created by taking the observed 30-day low-pass filtered tide gauge sea level value from the day the forecast is initialized and projecting it as a constant over the entire forecast period.

3.4.2 Propagation speed estimates

In order to generate an observation-based forecast, an estimated propagation speed is used to generate a sea level forecast based purely on propagation. The observation-based sea level forecast uses an estimated propagation speed to predict how fast the sea level upstream of the site of interest propagates to the site in question. The estimated planetary wave phase speed is generated using altimetry sea surface height data. Lag correlations are generated for each point of interest, i.e., both the Honolulu Harbor and Hilo tide gauge locations.

A lag-correlation analysis using the Pearson product-moment correlation coefficient (see Chapter 3.5.1) is used as a way to assess the propagation speed (Figure 3.3 and 3.4). The speed estimation is performed independently for the mesoscale and large-scale components of the altimetry data. Altimetry sea level data at the location of interest are correlated with sea level "upstream" (i.e., to the east) of the location for all lags up to 180 days. The lag-correlation analysis is performed for both Honolulu and Hilo (Figures 3.5 and 3.6), where the x-axis is the longitude (origin as the point of interest and upstream of the point of interest to the right), and the y-axis is the lag from day 0 to 180 days. For each lag, the longitude of the maximum correlation coefficient is identified (black circles in Figures 3.5 and 3.6). The best-fit slope of the maximum correlations in a linear regression is used as the propagation speed estimate for each location and spatial scale.

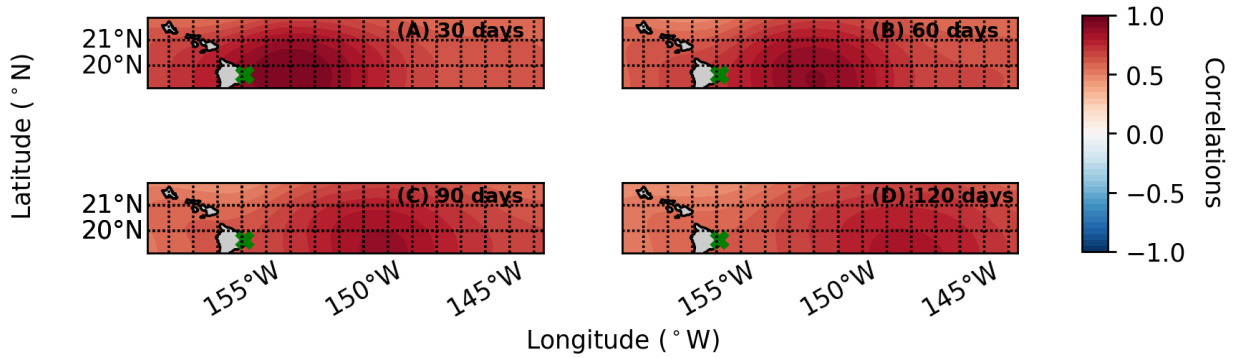

Figure 3.3: Mapped lag correlations of the 30-day low-pass filtered large scale altimetry sea level anomaly data at the latitude of the Hilo TG for spatial scales larger than 300 km at (A) 30, (B) 60, (C) 90, (D) 120 lag days. The green crosses are showing altimetry grid location of interest.

Large-scale sea level anomalies at the latitude of Hilo demonstrate clear propagation with extremely high lag correlations exceeding 0.75 out to long lags around 180 days (Figure 3.5, left). The estimated propagation speed for large-scale anomalies at the latitude of Hilo is 7.85 cm/s, which compares favorably to theoretical first-mode baroclinic wave speeds of about 7 cm/s at this latitude and observed speeds that tend to exceed theoretical (*Chelton and Schlax*, 1996). Mesoscale sea level anomalies at the latitude of Hilo also showed clear

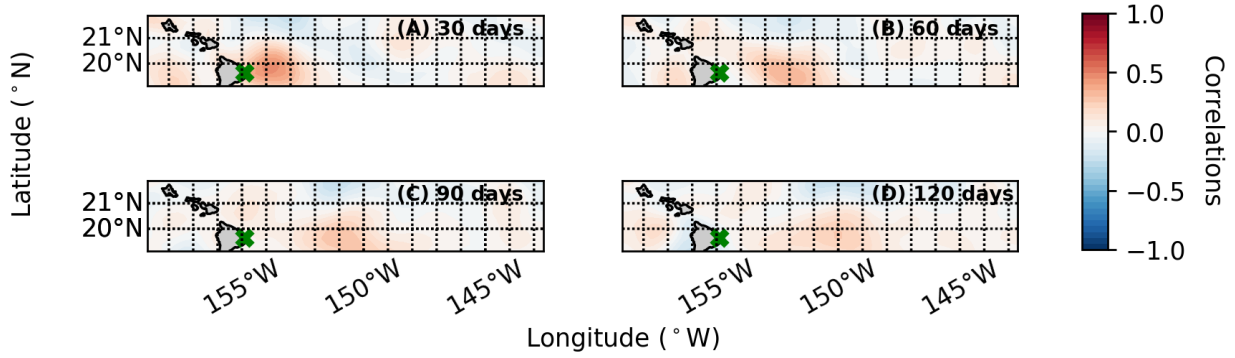

Figure 3.4: Mapped lag correlations of the 30-day low-pass filtered mesoscale altimetry sea level anomaly data at the latitude of the Hilo TG for spatial scales smaller than 300 km at (A) 30, (B) 60, (C) 90, (D) 120 lag days. The green crosses are showing altimetry grid location of interest.

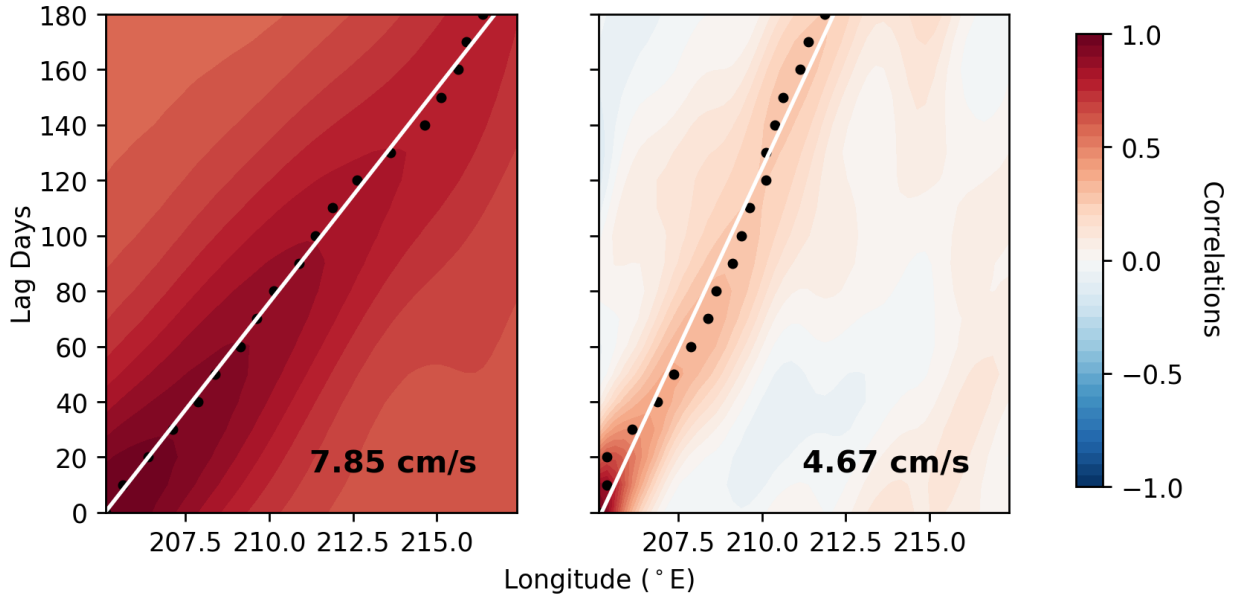

Figure 3.5: Lag correlations of the 30-day low pass filtered CMEMS altimetry sea level anomaly data at the latitude of the Hilo TG for spatial scales larger than 300 km (large scale, left) and spatial scales smaller than 300 km (mesoscale, right). The black dots are showing the maximum correlation at each 10-day increment lag, and the white line shows the line of best fit, which is used as the estimated propagation speed.

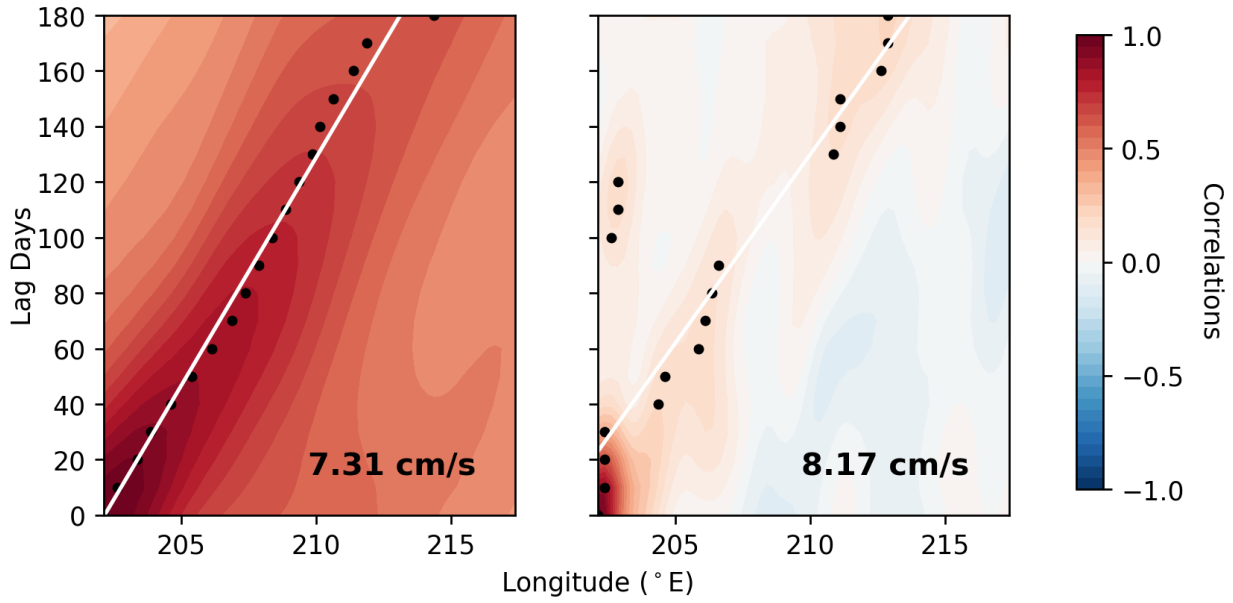

Figure 3.6: Lag correlations of the 30-day low pass filtered CMEMS altimetry sea level anomaly data at the latitude of the Honolulu Harbor TG for spatial scales larger than 300 km (large scale, top) and spatial scales smaller than 300 km (mesoscale, bottom). The black dots are showing the maximum correlation at each 10-day increment lag, and the white line shows the line of best fit, which is used as the estimated propagation speed.

propagation with a slower estimated speed of 4.67 cm/s (Figure 3.5, right). The estimated mesoscale speed is about 60% of the estimated large-scale speed, which may indicate that second-mode baroclinic propagation is important for the smaller spatial scales east of Hawaii Island. The theoretical second-mode speed is half that of the first baroclinic mode.

Large-scale anomalies at the latitude of Honolulu also demonstrate clear propagation with an estimated speed of 7.31 cm/s (Figure 3.6, left). The slightly slower speed compared to the latitude of Hilo is expected due to the decreasing local gradient in planetary vorticity, β, with increasing latitude. The lag correlations of these large-scale sea level anomalies are also quite high, though slightly reduced relative to the latitude of Hilo. In contrast, the correlations for the mesoscale sea level anomalies for Honolulu are much weaker, but there are signs of propagation (Figure 3.6, right). There is also a suggestion of local periodic variability from the non-zero correlations around lags of 100–120 days near the longitude of Honolulu. Taking into account the maximum correlations for the propagating portion of the

mesoscale anomalies (eliminating lead-days 100 to 120), the resulting propagation speed is estimated to be 8.17 cm/s, which is slightly faster than the estimated speed from correlations in the large-scale anomalies. It is important to note, however, that this speed is not likely to be robust due to the weak correlations and inconclusive structure in the lag-correlation analysis. There are signs of high correlation around the islands (Figure 3.6, right) at the longitude of the tide gauge and along the y-axis, indicating that the mesoscale variability appears to be have some locally generating properties.

3.4.3 Naïve propagation-based sea level forecasts

Using the estimated propagation speeds (Chapter 3.4.2), sea level forecasts are generated for each spatial scale independently by propagating anomalies from the east to the location of interest. For example, given an estimated propagation speed c, a forecast Δt days from initialization is created by assuming the sea level anomaly that is currently a distance $c\Delta t$ to the east will propagate unaltered to the location of the interest. Such forecasts are referred to herein as "naïve", because they assume the anomaly propagates undamped and unaltered by forcing along the path of propagation. One way to think about this type of naïve forecast is in the context of a simple one-dimensional 1.5-layer reduced-gravity model for which sea surface height (η) is described by the equation,

$$\frac{\partial \eta}{\partial t} - c_x \frac{\partial \eta}{\partial x} = \frac{\Delta \rho}{\rho} W_e - \lambda \eta, \tag{3.1}$$

where c_x is the zonal propagation speed (positive to the west), $\Delta\rho$ is the density difference between the surface layer and the interior, $W_e(x,t)$ is the Ekman pumping velocity, and λ is an inverse damping time-scale. In the case of the naïve forecast, we assume that the forcing and damping terms on the right-hand side are zero, and the forecast is completely determined by the initial conditions of the sea surface height field and the speed at which perturbations in the initial field propagate. In practice, including the forcing term is not practical due to

the lack of good predicted winds at seasonal time scales. Forecasts of the forcing term would be applicable no more than 10 days into the future if we are to use forecasted winds.

3.4.4 Optimized observation-based sea level forecast

$$\eta_{obs} = \kappa_p \tilde{\eta}_p + \kappa_l \tilde{\eta}_l + \kappa_m \tilde{\eta}_m + \epsilon, \tag{3.2}$$

where $\tilde{\eta}_p$ is a persistence forecast, $\tilde{\eta}_l$ and $\tilde{\eta}_m$ are naïve propagation-based sea level forecasts for the large-scale and mesoscale components, respectively, the κ parameters are the regression coefficients, and ϵ is the error in the forecast. In practice, the regression coefficients are estimated independently for each forecast length, Δt, by regressing the observed low-pass filtered tide gauge sea level anomalies, $\eta_{obs}(t)$, onto forecasts initialized from the altimetry data at times $t - \Delta t$.

To assess whether the optimization is sensitive to the particular set of years used to calculate the regression coefficients, the time frame of the altimetry data (1993–2018) are split into 500 distinct training and validation sets, where each training-validation pair is formed by randomly selecting six years for the validation set with the training set composed of the remaining twenty years. The linear regression coefficients for the persistence and naïve propagation forecasts are calculated for each lead day for each of the 500 training sets. The resultant linear regression coefficients vary as a function of lag as the relative importance of the persistence and naïve propagation-based forecasts changes (see Figure 3.7 and 3.8). The uncertainty about the regression coefficients (shown as the 68-percent or 1-sigma confidence interval) is calculated from the spread in the coefficients across the 500 training sets. The uncertainty is small, suggesting that the regression coefficients are robust and not sensitive to the particular set of years used to train the optimized observation-based forecast. The linear regression coefficients from each training set are then used to generate sea level "forecasts" (hindcasts in actuality) for the validation sets. The skill of the forecasts for the validation years is discussed in the following sections.

For a rough physical interpretation of the regression coefficients, it is instructive to return to the 1.5-layer model (Equation 3.1). Assuming that the forcing term is zero but retaining the damping term, then a method of characteristics solution for the 1.5-layer model in an ocean of infinite horizontal extent can be written

$$\eta(x,t) = e^{-\lambda\Delta t}\eta(x + c_x\Delta t, t - \Delta t), \tag{3.3}$$

where Δt is an arbitrary length of time in the evolution of the system. In the context of the observation-based sea level forecasts, Δt can be interpreted as a forecast length, and the right-hand side of the solution is identical to the naïve propagation-based sea level forecast modified by a damping factor. It is possible to then loosely interpret the components of the optimized forecast as damped versions of the naïve forecasts with the regression coefficients being related to the damping factor, $e^{-\lambda\Delta t}$, for each component. In the case of the persistence forecast, the speed c_x is zero.

3.5 Statistical evaluation of the forecasts

As mentioned in Chapter 3.4.1, the persistence forecast using the inverse barometer-corrected 30-day low-pass filtered tide gauge sea level data are used as a baseline of forecast performance and to assess the skill of the observation-based sea level forecast. Correlation coefficients and skill scores are specifically used to compare the persistence baseline and the observation-based sea level forecast in order to assess the skillfulness and the utility of the forecasts.

3.5.1 Pearson product-moment correlation coefficients

To calculate the correlation coefficients, the Pearson product-moment correlation coefficient (PPMCC) is used. PPMCC is a way to statistically measure the linear correlation between two variables and show the relation between the two in the means of strength and direction

(*Kiernan*, 2014). PPMCC is used to calculate the relation between the forecasted sea level and the observed sea level from the tide gauges. To calculate the correlation coefficients, the following equation is used

$$PPMCC = \frac{\Sigma(\eta_o - \overline{\eta_o})(\eta_f - \overline{\eta_f})}{\sqrt{\Sigma(\eta_o - \overline{\eta_o})^2}\sqrt{\Sigma(\eta_f - \overline{\eta_f})^2}}, \tag{3.4}$$

where η_o is the observed sea level, $\overline{\eta_o}$ is the mean of the observed sea level, η_f is the forecasted sea level, and the $\overline{\eta_f}$ is the mean of the forecasted sea level. Values of PPMCC vary from +1 to -1, with values near zero indicating a weak relationship between the two quantities. Positive values show positive linear correlation and the negative values are an indication of negative linear correlations.

The PPMCC is calculated between the observed tide gauge sea level and sea level from the optimized observation-based forecast, as well as the persistence and naïve propagation-based forecasts individually. The persistence forecast results are used as a performance baseline for the observation-based sea level forecasts. The PPMCC calculations are performed for forecast leads from 0 to 180 days, and the calculations are repeated for all 500 validation sets. The median and the 1-sigma (68 percent) confidence interval for the forecast correlation is plotted for assessment purposes (Figure 3.9 and 3.10, top).

A weakness of the PPMCC as a measure of calculating the skill of the forecast is that it ignores differences in the variance between the observational and forecasted sea level. The PPMCC shows the attainable skill of the forecast if the biases and variance are eliminated and could lead to overestimation of the forecast performance.

3.5.2 Brier skill score

As a more rigorous alternative to PPMCC, the Brier skill score offers a test for forecast skill that includes the effects of bias and differences in variance. The Brier skill score (BSS) is based on the mean square error (*Müller and von Storch*, 2004). BSS will only be equal

to PPMCC for absolute and conditionally unbiased skill. The BSS is calculated using the following equation

$$BSS = 1 - \frac{RMSE^2}{\sigma_r^2}, \tag{3.5}$$

where $RMSE$ is the root-mean-square error between the predicted and observed values (i.e., η_f and η_o, respectively), and σ_r^2 is the standard deviation of the observed values. The range of the BSS is $+1$ to $-\infty$, where a score of $+1$ indicates a perfect forecast result and a BSS of 0 and lower indicates there is no skill in the forecast.

Again, similar to the PPMCC, the BSS are calculated for the optimized observation-based forecasts, as well as the persistence and naïve propagation-based sea level forecasts individually. The BSS for all lags and validation sets are generated and plotted on a y-axis showing BSS between 0.0 and 1.0. The median and 1-sigma (68 percent) confidence interval of the BSS is plotted to evaluate the skillfulness of the sea level forecasts (Figure 3.9 and 3.10, bottom).

3.5.3 Correlation and skill of the forecasts

The regression coefficients for both Hilo and Honolulu suggest that up until about 20 days, the persistence forecast is the most effective component of the optimized forecast, while after 20 days the large-scale propagation component dominates (Figures 3.7 and 3.8). The mesoscale propagating anomalies receive little weight in the optimized forecast with regression coefficients that are much smaller compared to the other two components at all times. The variance in the regression coefficients is minimal over the 500 runs, suggesting that the coefficients are robust to the choice of data and are likely to be applicable for forecasting in an operational mode. In both cases, the regression coefficients for the large-scale propagation term are near one, suggesting little damping of the anomalies as they travel to the locations of interest. In contrast, the importance of the persistence term decays to near zero by about 40 days in both locations.

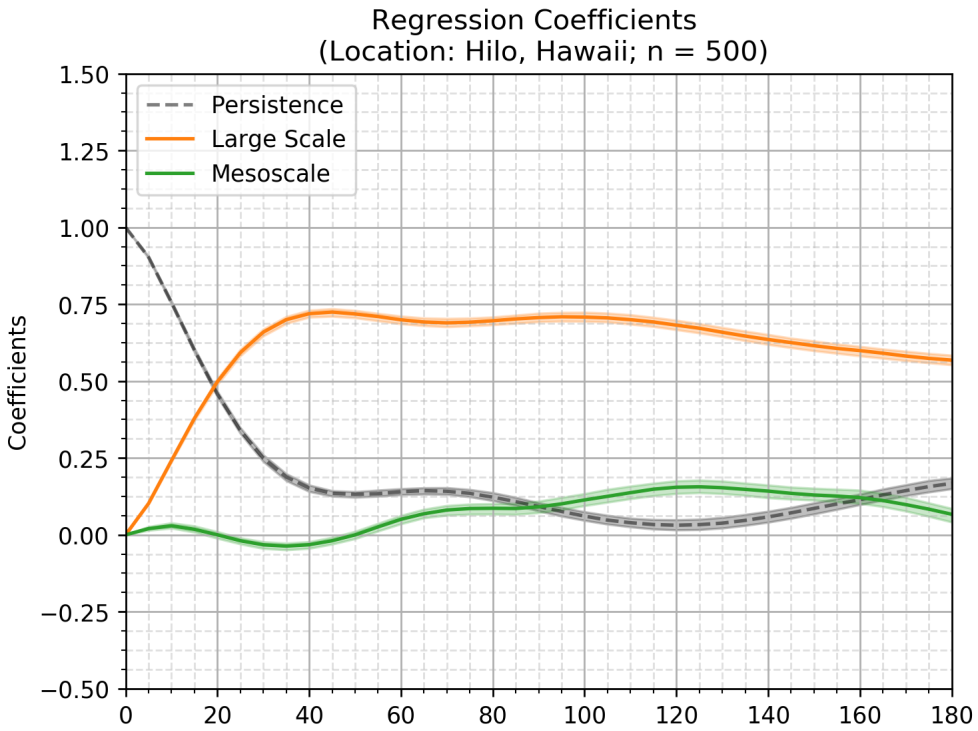

Figure 3.7: The calculated median linear regression coefficients for lead days 0 to 180 for Hilo are plotted with the 68% confidence interval (filled) of the 500 random runs. The persistence forecast used to generate the regression coefficients are from the 30-day low pass filtered TG sea level at each island. The large scale and mesoscale forecasts are from the 30-day low pass filtered CMEMS altimetry sea level at the closest altimetry point to the TG location. The relevance of the persistence and large scale forecast flips at around 20 days, and the mesoscale forecasts shows little contribution.

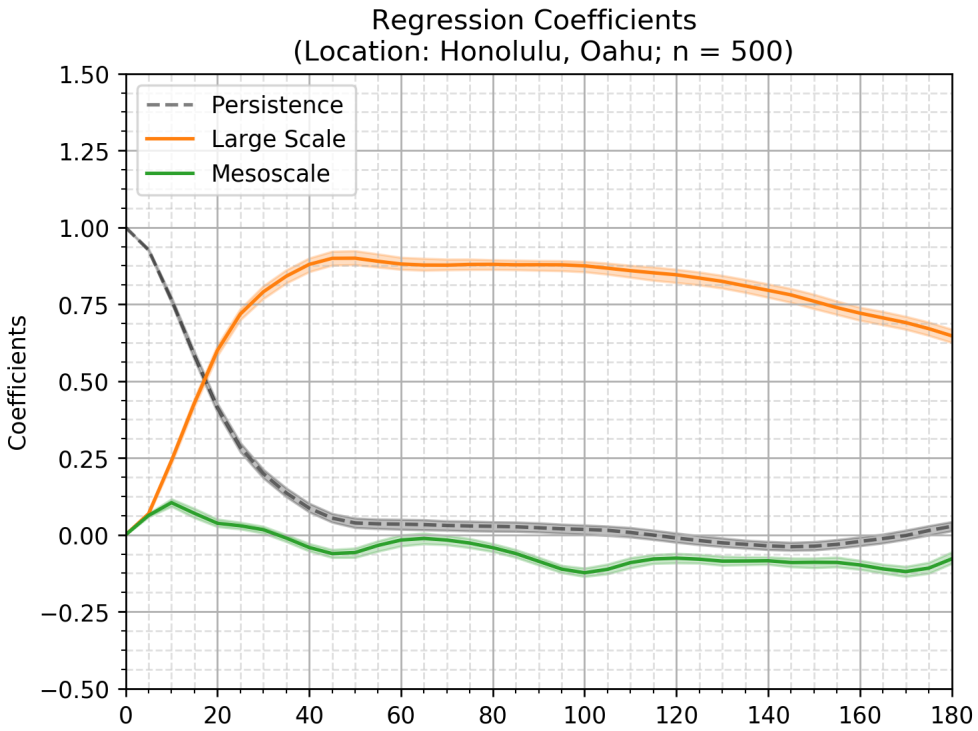

Figure 3.8: The calculated median linear regression coefficients for lead days 0 to 180 for Honolulu are plotted with the 68% confidence interval (filled) of the 500 random runs. The persistence forecast used to generate the regression coefficients are from the 30-day low pass filtered TG sea level at each island. The large scale and mesoscale forecasts are from the 30-day low pass filtered CMEMS altimetry sea level at the closest altimetry point to the TG location. The relevance of the persistence and large scale forecast flips at around 20 days, and the mesoscale forecasts shows little contribution.

Figures 3.9 and 3.10 show the results of the skill assessments for the Hilo and Honolulu Harbor tide gauge locations, respectively. These results suggest that both locations have comparable skill, which clearly beats naïve persistence at forecast leads of 30 days and longer. The median PPMCC for Hilo for the optimized observation-based forecast remains above 0.7 out to 100-day lead and above 0.6 for the entire 180-day forecast period (Figure 3.9, top). Compared to the baseline true naïve persistence forecast (dashed black line), after 30 days lead time, the optimized observation-based forecast (blue line) excels, but the performance is not statistically different and almost indistinguishable from the performance of the large-scale forecast (orange line). However, for the first 20 lead days, the large-scale forecast alone is significantly lower in skill compared to the persistence. Perhaps surprisingly, especially for Hilo, the mesoscale propagation forecast (green line) exhibits low skill as an independent predictor throughout the forecast timeframe of interest. The addition of the mesoscale sea level anomalies in the observation-based sea level forecasts does not add to skill of the observation-based sea level forecast. The primary components adding skill to the observation-based sea level forecasts are the persistence and large-scale propagation forecasts.

The bottom panels of Figures 3.9 and 3.10 show the skill calculated from the BSS for the forecasts at Hilo and Honolulu, respectively. The baseline persistence forecast possesses zero skill for leads longer than 60 days at both locations. In contrast, the skill for the optimized observation-based sea level forecasts is highly encouraging, showing results that are clearly better than persistence with skill scores of around 0.5 at 90-day lead times. Note that the BSS of the mesoscale propagation forecast drops below zero very quickly (within $\sim$10 days), indicating that the variance is mismatched between observations and forecasts at the mesoscale, and this component contributes little skill to the optimized forecast. The main contributions to the skill of the optimized forecast are persistence at short lead times and large-scale propagation at lead times of 30 days and longer.

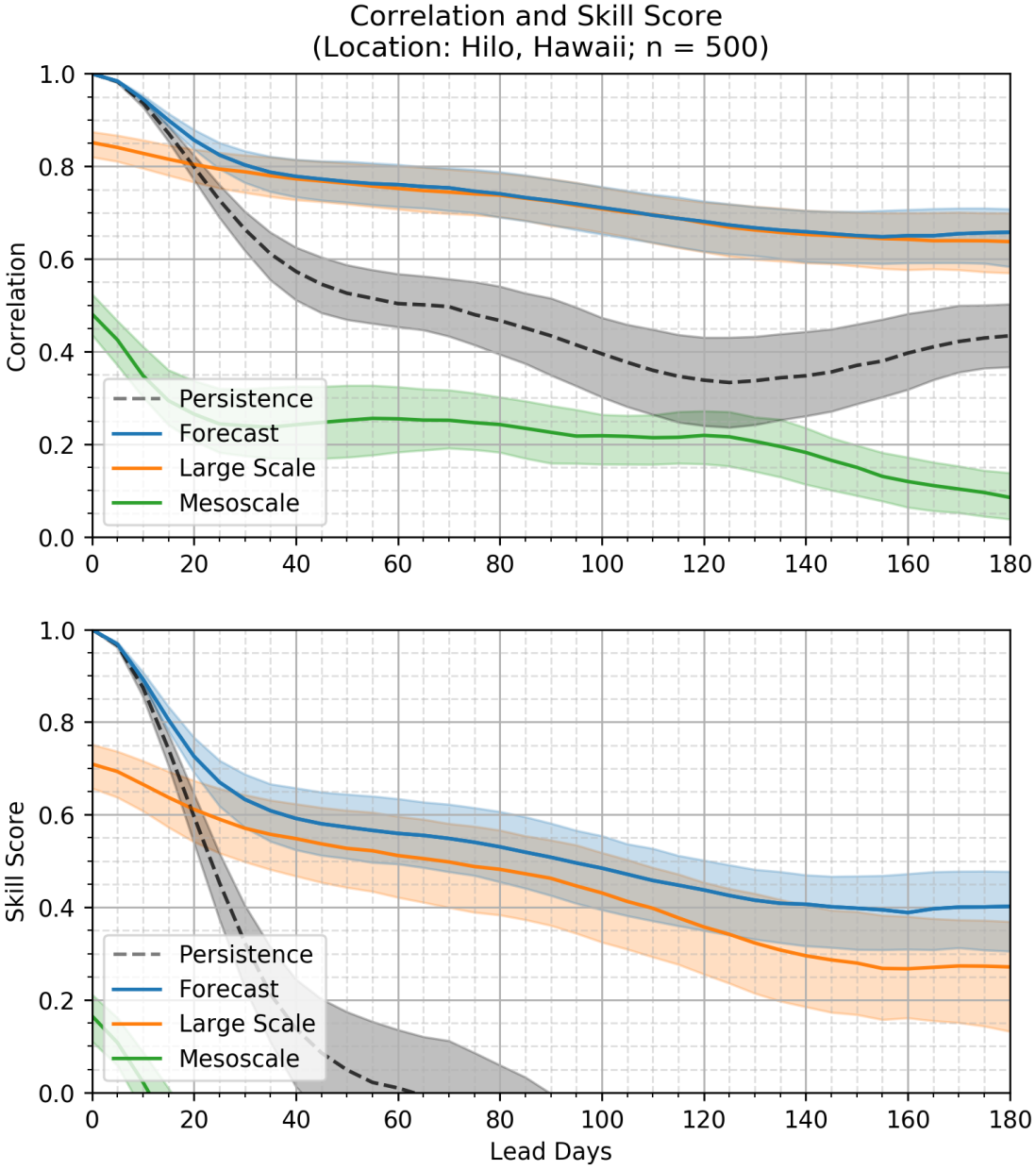

Figure 3.9: Statistical evaluation results of the observation-based sea-level forecast for Hilo, Hawaii for the 500 random runs. The median value of the observation-based sea level forecast (blue line) is compared to the baseline generated from true persistence (dashed black line). The observation-based components, large scale sea level forecast (orange line), and the mesoscale sea level forecast (green line) are also shown as individual forecasts. This figure also shows the 68% confidence intervals (filled) for each sea level forecast. Lead days as a function of PPMCC (top); lead days as a function of BSS (bottom). The results show that the observation-based sea level forecast exceeds the baseline forecasts results and there is little contribution from the mesoscale forecast.

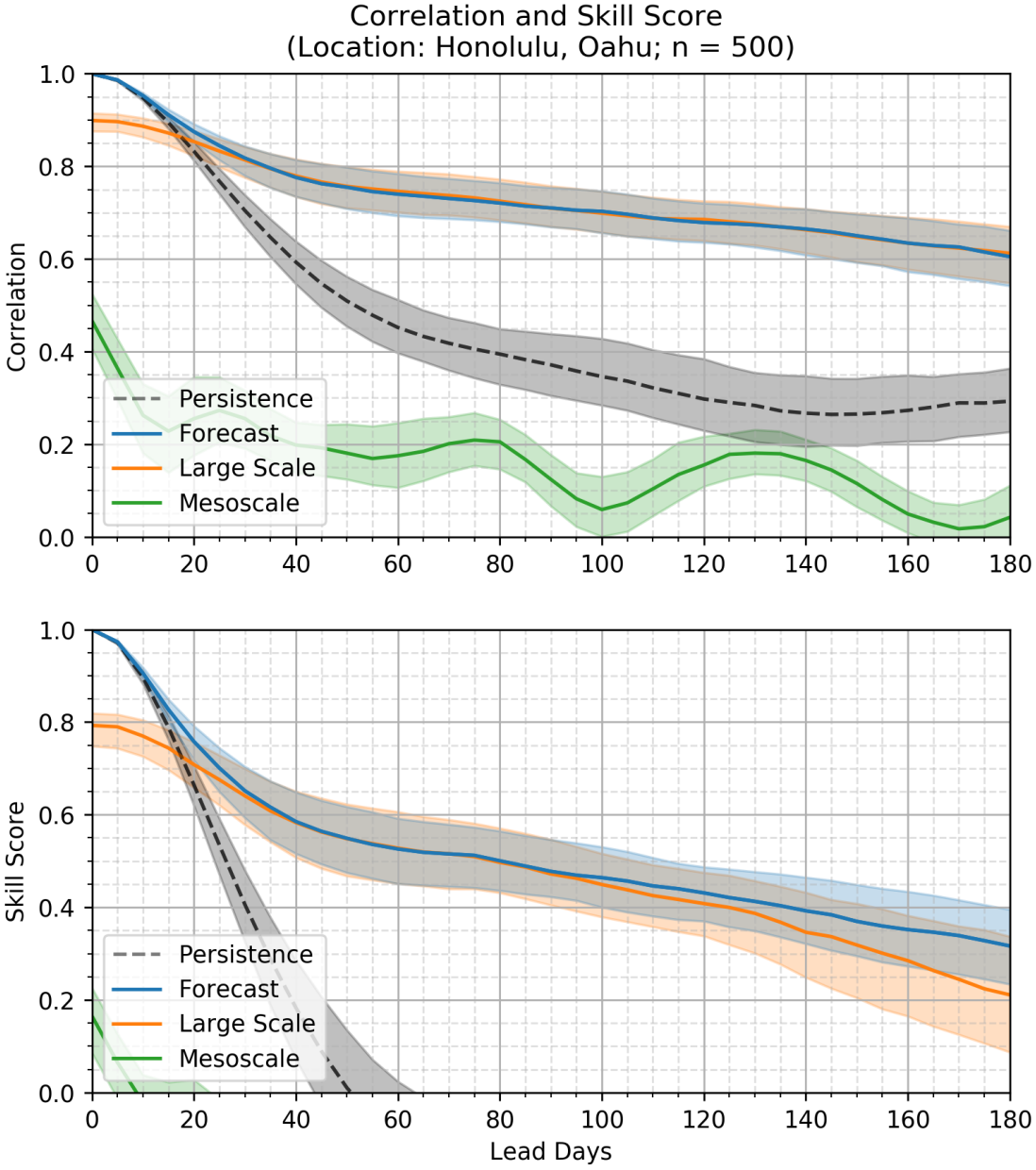

Figure 3.10: Statistical evaluation results of the observation-based sea-level forecast for Honolulu, Oahu for the 500 random runs. The median value of the observation-based sea level forecast (blue line) is compared to the baseline generated from true persistence (dashed black line). The observation-based components, large scale sea level forecast (orange line), and the mesoscale sea level forecast (green line) are also shown as individual forecasts. This figure also shows the 68% confidence intervals (filled) for each sea level forecast. Lead days as a function of PPMCC (top); lead days as a function of BSS (bottom). The results show that the observation-based sea level forecast exceeds the baseline forecasts results and there is little contribution from the mesoscale forecast.

3.6 Operational observation-based sea level forecasts

The mesoscale components of the forecasts do not contribute significantly to forecast skill at either Hilo or Honolulu. As seen earlier in Table 2.1, the mesoscale sea level variability has more relevance in Honolulu (16% of overall daily sea level variance), and it is possible that the overall forecast skill is slightly lower at Honolulu due to the lack of mesoscale forecast skill. As for Hilo, Figure 3.5 (right) suggested forecast skill from clear propagating features; however, the optimized observation-based sea level forecast did not give significant weight to the mesoscale forecasts. It could be that the sea level variability contribution in the mesoscale is simply too small in Hilo (about 9% of the overall daily sea level variance) to factor heavily into the forecast. Therefore, for the Hawaiian Islands, the mesoscale variability could be ignored. We suggest, however, that future work focus on assessing methods to increase the skill of the mesoscale component. Finally, for the study presented here, the research quality CMEMS altimetry data was used. Operationally, the near-real-time CMEMS altimetry data would have to be used to generate near-real-time daily sea level forecasts. It is not known at this time if using the near-real-time data would affect the skill of the forecasts.

Chapter 4

Seasonal forecasts of high-tide flooding

Open-ocean sea level observations from satellite altimetry correspond to coastal sea level variability observed by tide gauges in Hawaii at periods longer than about 30 days (Section 2.7). As a result, the mean sea level forecasts developed here (Section 3.4.4) are applicable at monthly timescales out to about 6 months. Monthly mean sea level anomalies make up a relatively small fraction of the overall hourly sea level variance in Hawaii, but the low-frequency variations change the baseline around which higher-frequency anomalies and tidal variations occur. For example, monthly mean sea level anomalies in Hilo can determine the difference between having zero or many exceedances above a threshold during a given month (Figure 2.9). Thus, the primary utility of these forecasts is not in the ability to predict the mean sea level anomalies themselves, but rather the ability to forecast periods in which the likelihood of high-tide flooding (HTF) is enhanced or reduced. The summer of 2017 and the unprecedented number of HTF events in Honolulu (Chapter 1) is a primary motivator of this work. An important test of the utility of these forecasts is to evaluate whether the observation-based sea level forecasts could have predicted the enhanced number of events during that time.

Relating forecasts of monthly mean sea level to expected monthly counts of HTF days is achieved via an updated version of the hierarchical statistical model developed in *Thompson et al.* (2019), with the most notable update being a switch from annual resolution to independent models for each calendar month of the year. Note that a HTF day is defined

to be a day in which at least one hourly sea level value exceeds the flooding threshold of interest. The fundamental assertion of the *Thompson et al.* (2019) statistical model is that the probability mass distribution governing the number of HTF days at a given location during a given period is closely related to a single parameter,

$$\Delta_{99} \equiv (\zeta_{99} + \bar{\eta}) - H \tag{4.1}$$

where ζ_{99} is the 99th percentile of predicted astronomical tidal heights relative to current tidal datums, $\bar{\eta}$ is the mean of the nontidal sea level variability over the period in question (in this case a single month), and H is the height of the flooding threshold of interest. The term in parentheses, $(\zeta_{99} + \bar{\eta})$, provides a general measure of the height of high tides during a given month. The specific role of ζ_{99} is to capture variability in high-tide levels due to seasonal-to-decadal modulations in tidal range. The specific role of $\bar{\eta}$ is to capture variability in high-tide levels due to changes in the mean level (both secular and stochastic) about which the astronomical tides vary. By subtracting the threshold height, H, from this sum, we can interpret variability in Δ_{99} as a measure of whether high tides are generally higher (more positive Δ_{99}) or lower (more negative Δ_{99}) compared to the threshold for a given period of time. If we also consider the presence of stochastic sub-monthly processes, then we can state more formally that the parameter is related to the probability mass distribution (PMD) of the number of daily high tides that exceed the threshold during a month. *Thompson et al.* (2019) utilized a beta-binomial distribution to capture the wide variety of distribution shapes that are needed to describe how the distribution changes with Δ_{99}. The shape of the beta-binomial distribution is determined by a set of parameters, which, in practice, are related to Δ_{99} by prescribed functional forms that are conditioned on observed values of Δ_{99} and counts of HTF days from tide gauge observations. The details of this conditioning process are described in greater detail in *Thompson et al.* (2019) and remain largely the same in the present analysis. The outcome of this statistical model is an algorithm that accepts a

value (or distribution of values) for Δ_{99} in a given month and returns a probability mass distribution for the number of HTF days that can be expected given Δ_{99}.

The interface between the monthly mean sea level forecasts and the statistical model for monthly counts of HTF days occurs via $\bar{\eta}$ in the definition of Δ_{99}. However, the mean sea level forecasts produce estimates of anomalies relative to the multidecadal trend and mean annual cycle calculated over the altimetry period, 1993–2019. These components must be added back to the forecasts of mean sea level anomalies to produce accurate forecasts of HTF days. In addition, there is uncertainty associated with the forecasted monthly mean sea level anomalies that must be propagated into the forecasts of HTF days. In practice, we treat this uncertainty as normally distributed white noise with a standard deviation equal to the standard deviation of differences between observed and retrospectively forecasted monthly mean sea level anomalies during the altimetry period (σ_ϵ). In the following analysis, we generate retrospective three-month and six-month outlooks for numbers of HTF days and compare to observed counts of HTF days over the same periods from tide gauge data.

The procedure for generating three-month and six-month outlooks for numbers of HTF days is as follows:

1. Initialize retrospective mean sea level forecasts on the 15th day of each calendar month, which allows the 30-day low-pass filter to produce estimates of monthly mean sea level for the month with minimal contributions from edge effects.

2. Produce forecasts of monthly mean sea level anomalies for the subsequent 6 months using the procedure outlined in Chapter 3. E.g., for a forecast initialized on January 15th, forecasts of monthly mean sea level are produced for February through July.

3. The multidecadal trend and mean annual cycle during the altimeter period are added to the forecasted anomalies, and the resulting monthly mean sea level is adjusted to be relative to the mean sea level datum of the tide gauge.

4. For each month during the forecast period, the statistical algorithm for HTF days receives four inputs: monthly mean sea level from the previous step in this procedure, uncertainty in the mean sea level forecast (σ_ϵ), ζ_{99} over the forecast month calculated from the official NOAA tidal prediction, and a threshold of interest (H).

5. Output of the statistical model is used to generate retrospective three-month and six-month HTF forecasts composed of a "best guess" and a likely range (17th to 83rd percentile) for the total number of HTF days expected over the three- and six-month periods following the forecast initialization date.

Using this procedure, retrospective forecasts of HTF days were initialized for every month in the altimeter record. Three-month and six-month forecasts of HTF days exceeding 30 cm above MHHW in Hilo compare favorably with the observed number of HTF days over the same three- and six-month periods (Figure 4.1). For the largest observed counts, the numbers of observed HTF days fall within the likely range of the forecasted counts (i.e., the gray vertical bars intersect the black diagonal 1:1 line). Note that the comparisons are similarly favorable for other thresholds as well. Forecasts for Honolulu (not shown) do not compare favorably with the observed counts. The reason for the discrepancies in Honolulu are not yet clear, but it does not appear to be related to lack of skill in the mean sea level forecasts. Rather, the statistical model relating mean sea level to numbers of HTF days does not perform adequately during the particular months (many during 2017) when the largest numbers of HTF days occur. Understanding the shortcomings of the statistical model in Honolulu during these particular months will be the subject of future work.

Returning to the unprecedented year of 2017, the largest observed three-month count in Hilo (14 HTF days) corresponds to November 2017 through January 2018, and the second largest observed three-month count (13 HTF days) corresponds to May–July, 2017 (as denoted in Figure 4.1a). The forecasts for these three-month periods—initialized on April 15th and October 15th, respectively—accurately predict the numbers of HTF days, with the observed counts falling well within the likely range in both cases. The same goes for largest

six-month counts in Hilo (18 HTF days) that occurred during April–September, 2017 (Figure 4.1b). Thus, had this forecast system been operational, advanced warning of the impacts of high-tide flooding in Hilo during 2017 could have been provided to those managing coastal resources and infrastructure. This suggests that observation-based sea level forecasts can be an effective tool for mitigating against the impacts of high-tide flooding as the frequency of such flooding increases with sea level rise.

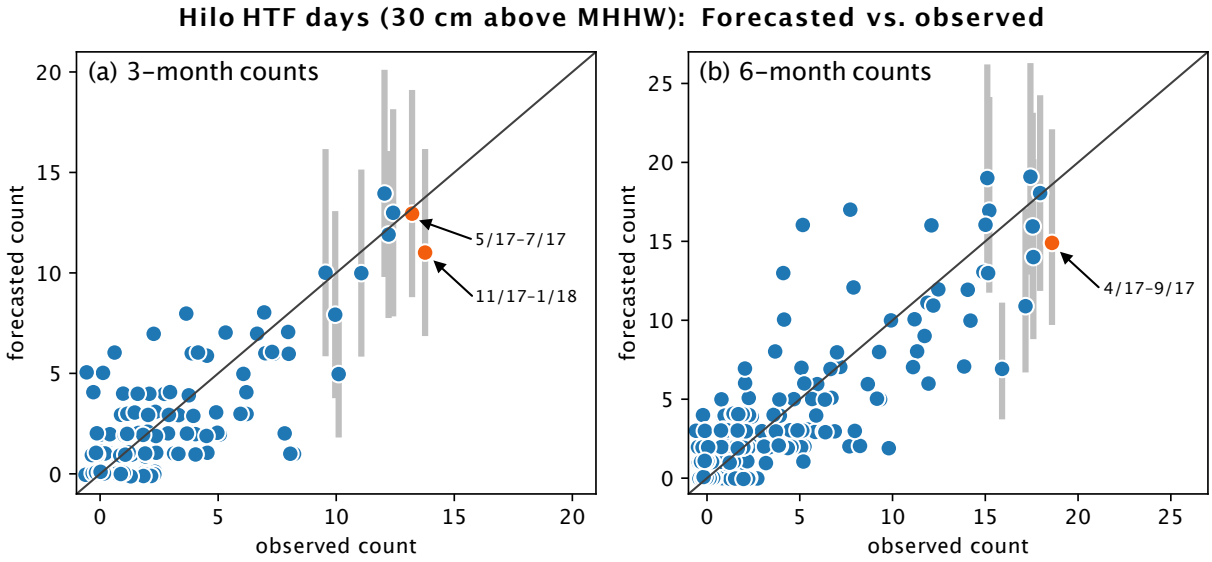

Figure 4.1: Comparisons of forecasted and observed counts of HTF days in Hilo (30 cm above MHHW) during three- and six-month intervals (left and right, respectively) since the beginning of the altimeter record in 1993. Likely ranges (17th to 83rd percentiles) about the forecasted counts are shown as vertical gray bars. Likely ranges are shown only for the largest observed counts each panel to avoid cluttering the figure. A small amount of random scattering is applied to the markers to allow multiple markers to be seen where many are co-located.

Chapter 5

Discussion and conclusions

5.1 Impact of seasonality

The observation-based mean sea level forecast (Chapter 3) did not attempt to account for seasonal differences in propagation speeds or seasonal changes in the relative importance of the forecast components. There are, however, clear seasonal differences in the oceanographic and atmospheric conditions around the Hawaiian Islands, and the seasonal changes vary greatly even over the small latitudinal differences between the locations of Hilo and Honolulu. To illustrate the seasonal variability, climatologies of zonal currents (Figure 5.1) and wind-stress (Figure 5.2) were computed from the $1^\circ \times 1^\circ$ gridded ocean reanalysis, Ocean ReAnalysis System 5 (ORAS5) from ECMWF. Such seasonal differences could affect the observation-based sea level forecast due to small changes in propagation speeds or the impact of differences in wind-forcing from one season to the next.

Figure 5.3 shows the standard deviation of the difference between inverse barometer-corrected 30-day low-pass filtered observed tide gauge sea level and the forecasted sea level from the observation-based forecast at various leads. The standard deviation of the forecast differences are lower in the fall season (September–October) for Hilo, Hawaii, while no clear seasonal differences are apparent for Honolulu. While not conclusive, there is a possibility that training the model for specific seasons could produce improved skill from the observation-based sea level forecast.

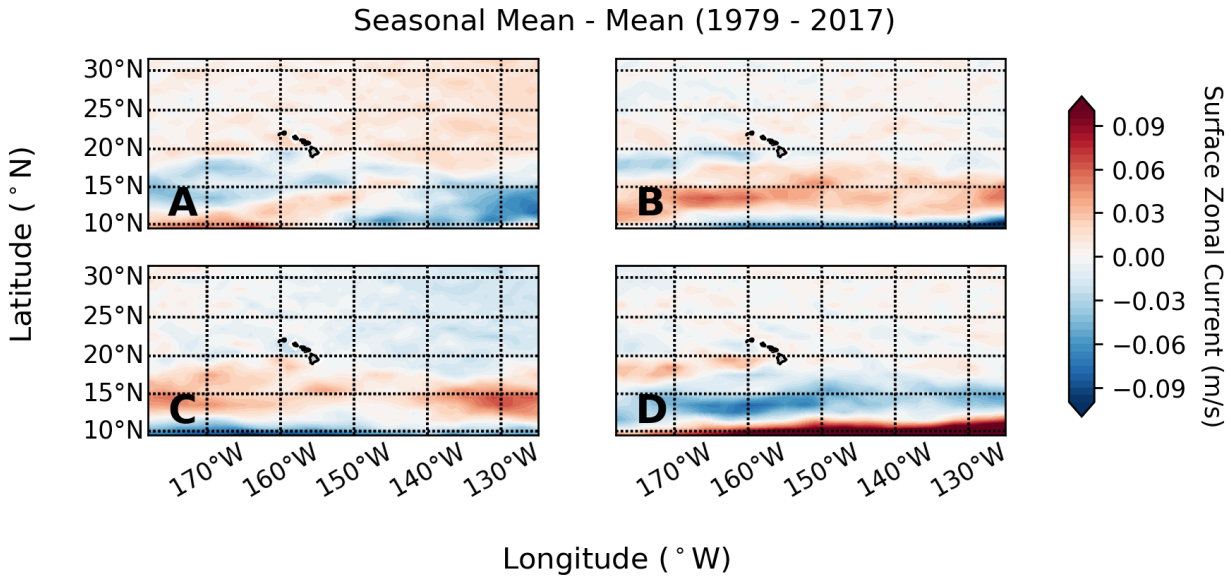

Figure 5.1: ORAS5 seasonal mean surface zonal current where the overall mean is removed for (A) winter, (B) spring, (C) summer, and (D) fall. There are signs of strengthened zonal flow in fall (son, D) and possibly winter (djf, A) at the latitudes of Hawaii.

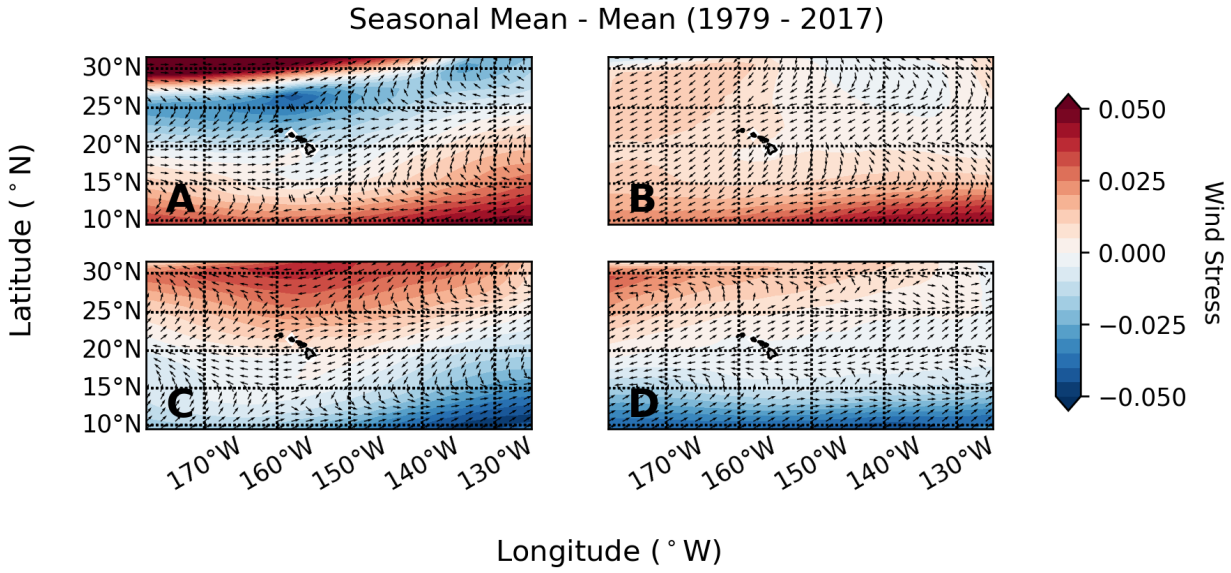

Figure 5.2: ORAS5 seasonal mean windstress where the overall mean is removed for (A) winter, (B) spring, (C) summer, and (D) fall.

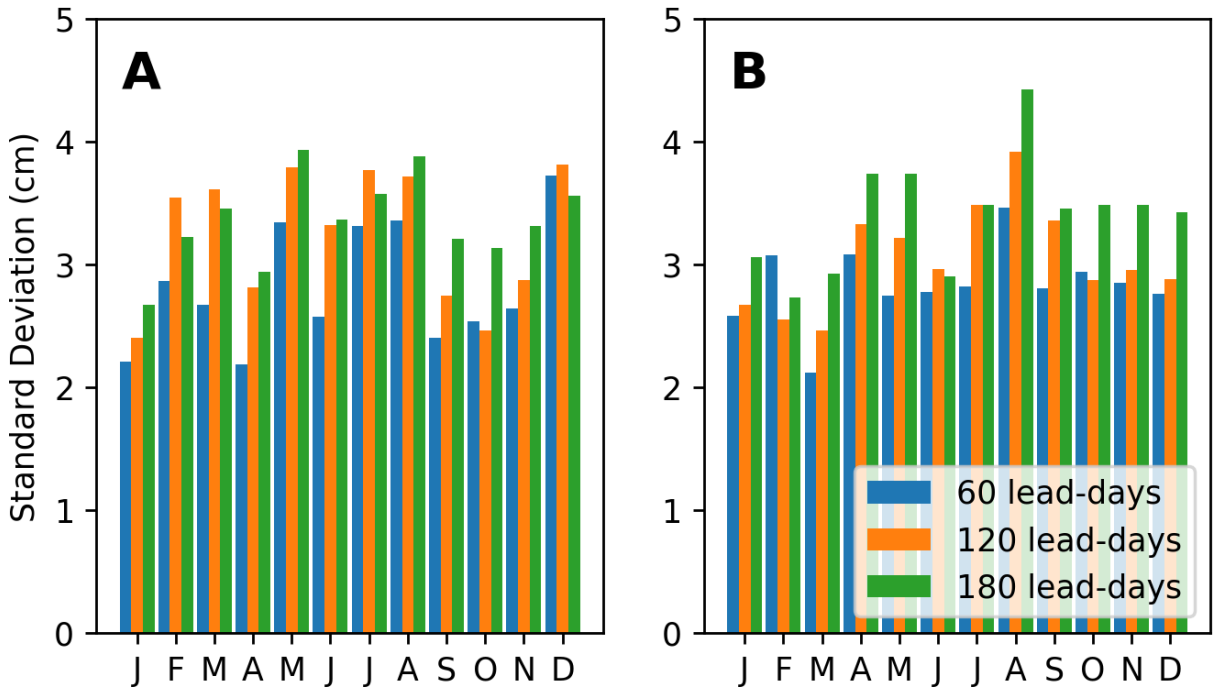

Figure 5.3: Standard deviation of the difference between 30-day low-passed observed TG sea level and forecasted sea level from the observation-based sea level forecast for (A) Hilo and (B) Honolulu. Fall season (son) for Hilo seems to have slightly low standard deviation compared to the other seasons, showing indication of potential increase in forecast skill for Hilo in the fall season.

Seasons (months)	Hilo (cm/s)		Honolulu (cm/s)	
	Large scale	Mesoscale	Large scale	Mesoscale
Full record	7.85	4.67	7.31	8.17
Winter (djf)	7.17	4.68	8.46	7.35
Spring (mam)	8.91	4.80	5.46	5.45
Summer (jja)	6.64	5.78	8.14	9.24
Fall (son)	8.33	6.27	7.31	7.61

Table 5.1: Calculated propagation speeds

5.1.1 Propagation speeds and forecasts by season

With the seasonal observation-based forecast, the idea is to divide the year into four seasons and generate sea level forecasts specifically for each season. The initial test was to see if the propagation speeds for the large-scale and mesoscale height anomalies calculated from the lag-correlation analysis (Chapter 3.4.2) varied if calculated on a seasonal basis. The year was separated into four seasons: winter (December–February), spring (March–May), summer (June–August), and fall (September–November). Figures 5.4 and 5.5 show the lag-correlation analysis and estimated propagation speeds for large-scale and mesoscale sea level anomalies, respectively, at the latitude of Hilo. The seasonally calculated propagation speeds for large and mesoscale sea level anomalies show that there are variations in the estimated speeds that could affect the skill of the sea level forecasts. With the exception of the spring season, estimates of the large-scale propagation speeds (Figure 5.4) are well-constrained with clear propagation structure in the lag-correlation analysis and speeds varying up to 30% from 6.64 cm/s up to 8.33 cm/s. The large-scale propagating anomalies are most tightly correlated in the fall, and the propagation speed is faster in fall compared to winter and summer. The structure of mesoscale propagation in the seasonal lag-correlation analysis (Figure 5.5) is much less clear compared to the previous analysis ignoring seasonal differences. As a result, it was less clear for some seasons how to identify structure in the lag-correlation analysis to calculate speeds. Regardless, an attempt was made for each season in order to produce optimized observation-based forecasts as in the full-record calculations in Chapter 3.4.

The optimized observed-based forecast procedure, including the training-validation subsetting, was repeated for each season individually. The regression coefficients did differ amongst the four seasons (not shown), but the differences were small, and the coefficients were comparable to the non-seasonal results. As in the non-seasonal analysis, persistence dominated at short lead times, large-scale propagation dominated at longer lead days, and the mesoscale propagating anomalies showed little contribution. Similarly, the variance in

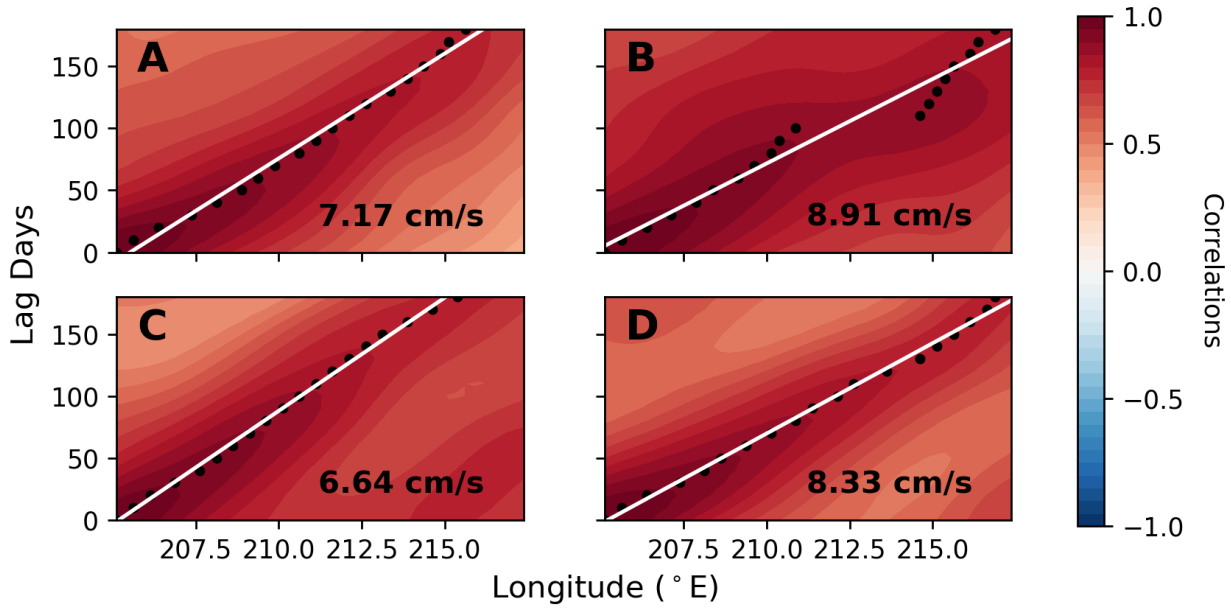

Figure 5.4: Lag correlations of the 30-day low-pass filtered CMEMS altimetry sea level anomaly data at the latitude of the Hilo TG for spatial scales larger than 300 km (large scale) where the sea level data have been separated seasonally to (A) winter, (B) spring, (C) summer, and (D) fall. The black dots are showing the maximum correlation at each 10-day increment lag, and the white line shows the line of best fit, which is used as the estimated propagation speed. The large scale sea level anomalies show signs of propagation, where the propagation speed is the fastest in the summer (6.64 cm/s), and slowest in the fall (8.33 cm/s). Note that the propagation speed using non-seasonally separated sea level data, the propagation speed of large scale sea level anomalies was 7.85 cm/s (Figure 10, left).

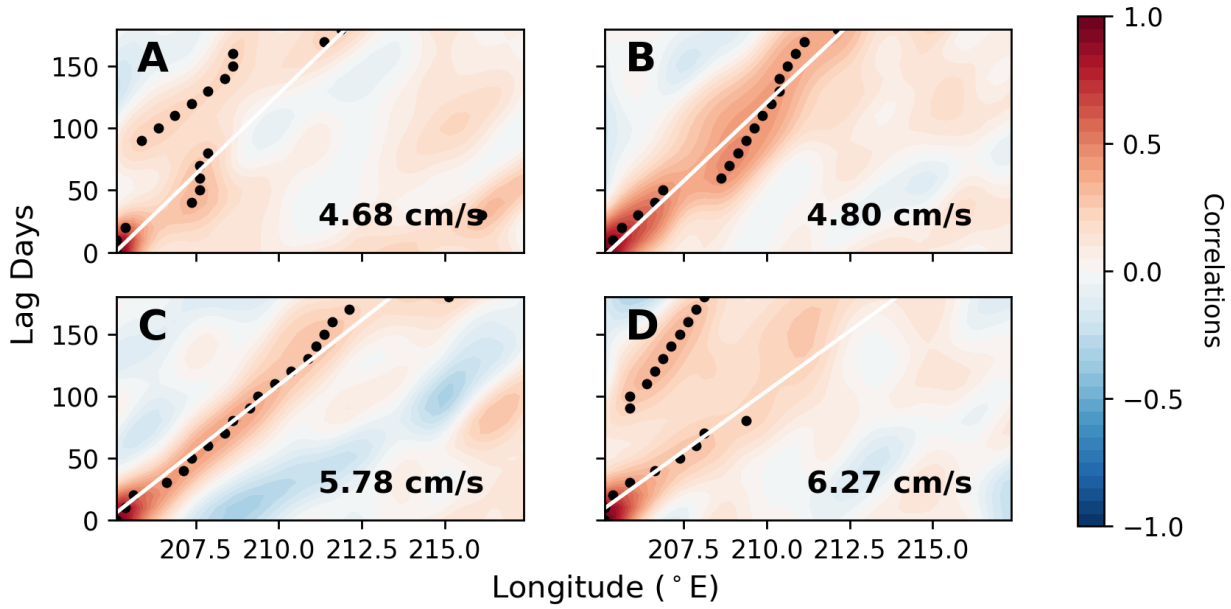

Figure 5.5: Lag correlations of the 30-day low pass filtered CMEMS altimetry sea level anomaly data at the latitude of the Hilo TG for spatial scales smaller than 300 km (mesoscale) where the sea level data have been separated seasonally to (A) winter, (B) spring, (C) summer, and (D) fall. The black dots are showing the maximum correlation at each 10-day increment lag, and the white line shows the line of best fit, which is used as the estimated propagation speed. Overall, the mesoscale sea level anomalies show signs of propagation, however the propagating features are most clear in spring and summer. Note that the propagation of the mesoscale anomalies were cleas when using non-seasonally separated sea level data, the propagation speed of mesoscale sea level anomalies was 4.67 cm/s (Figure 10, right).

the regression coefficients were well-constrained and showed minimal spread across the 500 training sets.

5.1.2 Results of splitting forecasts by season

Consistent with the non-seasonal sea level forecast (Figure 5.6, solid black line), the seasonal observation-based sea level forecasts exhibited high potential skill at the Hilo tide gauge location for all seasons, far exceeding the skill of the persistence forecasts (Figure 5.6, dotted lines). Interestingly, the fall season is the only season to stand out as having significantly more skill than the non-seasonal forecasts. The median PPMCC for the fall season exceeded 0.8 out to 160 lead days (Figure 5.6, solid purple line), and the BSS exceeded 0.6 out to 100 days (Figure 5.7, solid purple line). However, overall, there is no significant advantage in adding seasonality to the propagation-based sea level forecast over the non-seasonal data at Hilo other than for the fall season. The results were similar for Honolulu, where the forecast skill did not appreciably increase for any season relative to using the complete record (not shown).

5.2 The role of mesoscale sea level variability

The results from the observation-based sea level forecast were unable to leverage any substantial predictability from the mesoscale sea level variability despite an overall large contribution to variance in multiple regions surrounding the Hawaiian Islands (Figure 2.4). One obvious limitation of the observed-based forecast methodology is the assumption of purely zonal propagation, which may have hindered the ability of mesoscale variability to factor heavily in the optimization. As shown in Table 2.1, mesoscale variability constitutes a significant fraction of daily sea level variance, and multiple studies have highlighted the important role of mesoscale eddies in the largest coastal sea level extremes observed in Hawaii (*Firing and Merrifield*, 2004; *Yoon et al.*, 2018). Moreover, these are not isolated cases, as *Fir-*

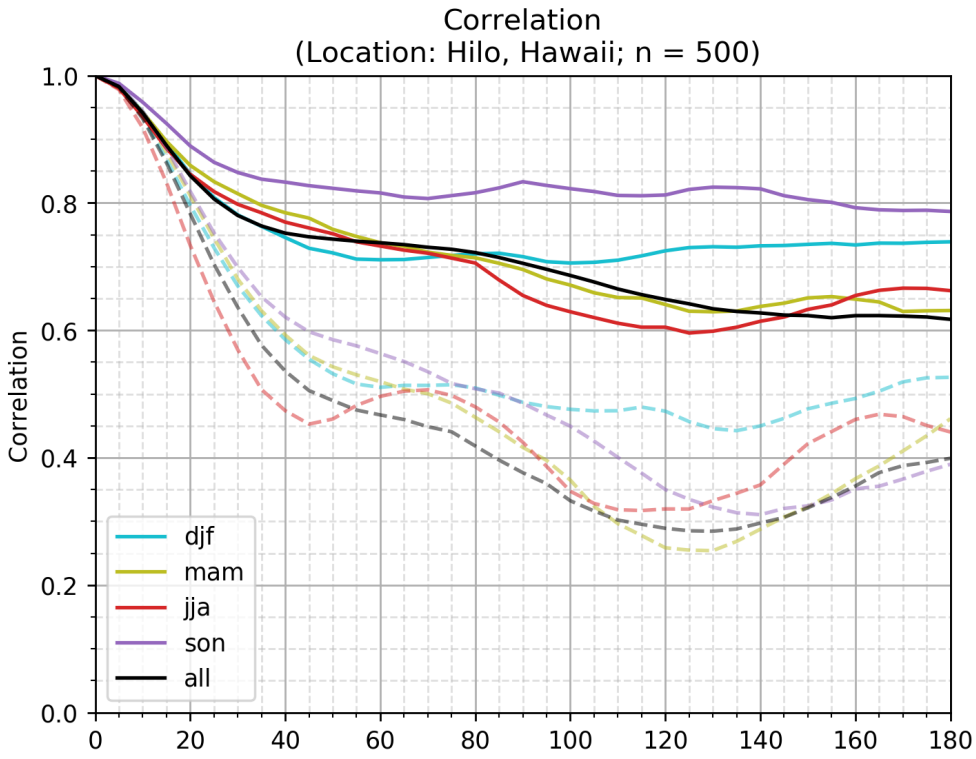

Figure 5.6: Lead days as a function of potential skill (PPMCC) of the observation-based sea-level forecast and persistence for Hilo, Hawaii for the 500 random runs with seasonal differences. The median value of the seasonal and non-seasonal observation-based sea level forecast (solid lines) is compared to the baseline generated from persistence (dashed lines). The black lines are the non-seasonal observation-based sea level forecast results to compare with the seasonal results, to identify if there is any relevance in including the seasonal differences. The results show that the seasonal observation-based sea level forecast only exceeds the non-seasonal forecasts for the fall season (son, purple solid line) and there is little relevance in seasonally forecasting for the other seasons.

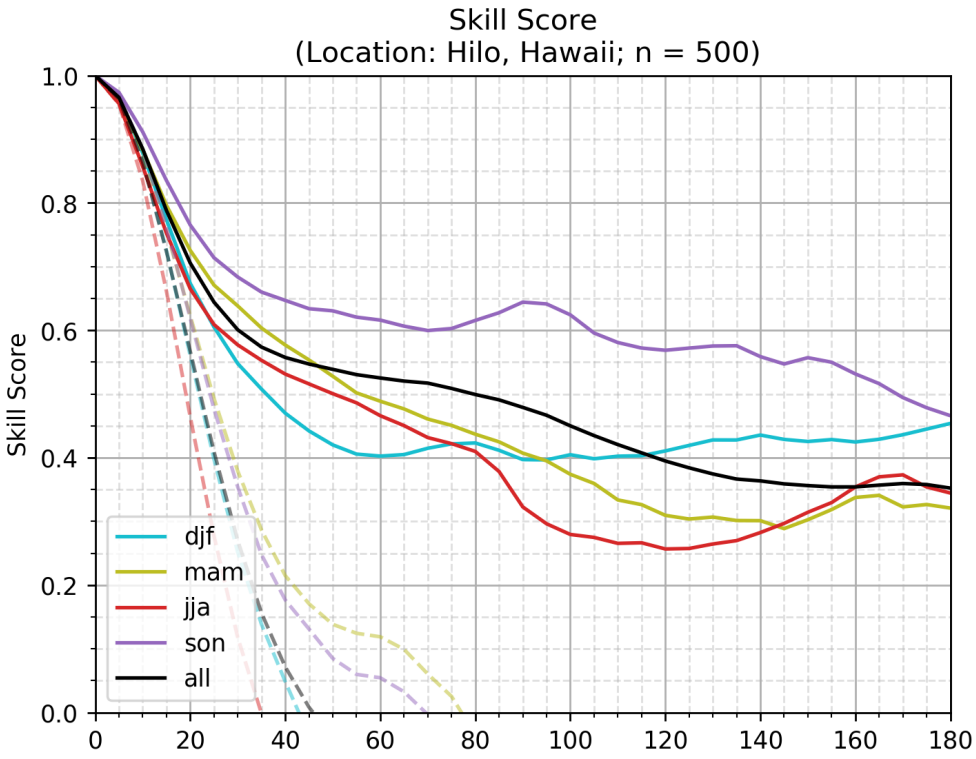

Figure 5.7: Lead days as a function of BSS of the observation-based sea-level forecast and persistence for Hilo, Hawaii for the 500 random runs with seasonal differences. The median value of the seasonal and non-seasonal observation-based sea level forecast (solid lines) is compared to the baseline generated from persistence (dashed lines). The black lines are the non-seasonal observation-based sea level forecast results to compare with the seasonal results, to identify if there is any relevance in including the seasonal differences. The results show that the seasonal observation-based sea level forecast only exceeds the non-seasonal forecasts for the fall season (son, purple solid line) and there is little relevance in seasonally forecasting for the other seasons.

ing and Merrifield (2004) found that between 1993 and 2004, there were approximately 10 large (>15 cm) anticyclonic eddies that reached the Hawaiian Islands and observed that extreme sea levels tend to occur when the eddies reach the Hawaiian Islands during the summer season. Given the clear impact of mesoscale eddies on coastal sea level, the region of substantially reduced RMS sea surface height variability following the topography of the Hawaiian Ridge (Figure 2.4) is most puzzling. Thus, the dynamics of how and under what conditions mesoscale eddies significantly affect coastal sea level in Hawaii is an important area of future research. In the medium-term, exploring ways to relax the assumption of purely zonal propagation may improve the observation-based forecasts by better capturing the influence of mesoscale eddies.

5.3 Skill comparison: Observation-based vs dynamical models

As discussed in Chapter 1, the currently available dynamical forecast models are not particularly skillful in predicting monthly sea level at the latitude of Hawaii. In order to assess how the dynamical models compare to the observation-based sea level forecast, the skill of observation-based forecasts in Honolulu was compared to results from a multimodel analysis of sea level forecasts from operational dynamical models (obtained via personal communication with Xiaoyu Long and Matthew Widlansky). Figure 5.8 shows the forecast skill for Honolulu sea level from various operational dynamical forecast models (colored lines) compared to the skill of the observation-based forecast developed here (black line with dots). The figure specifically shows skill for forecasts initialized in April, i.e., prior to the spring barrier in predictability. The skill measure in this case is correlation between observed monthly mean tide gauge anomalies with trend and annual cycle removed (inverted barometer effect not removed). Note that the observation-based forecasts were made up to 180 lead-time, i.e., 6 months, whereas the dynamical models were forecasted for 11 months.

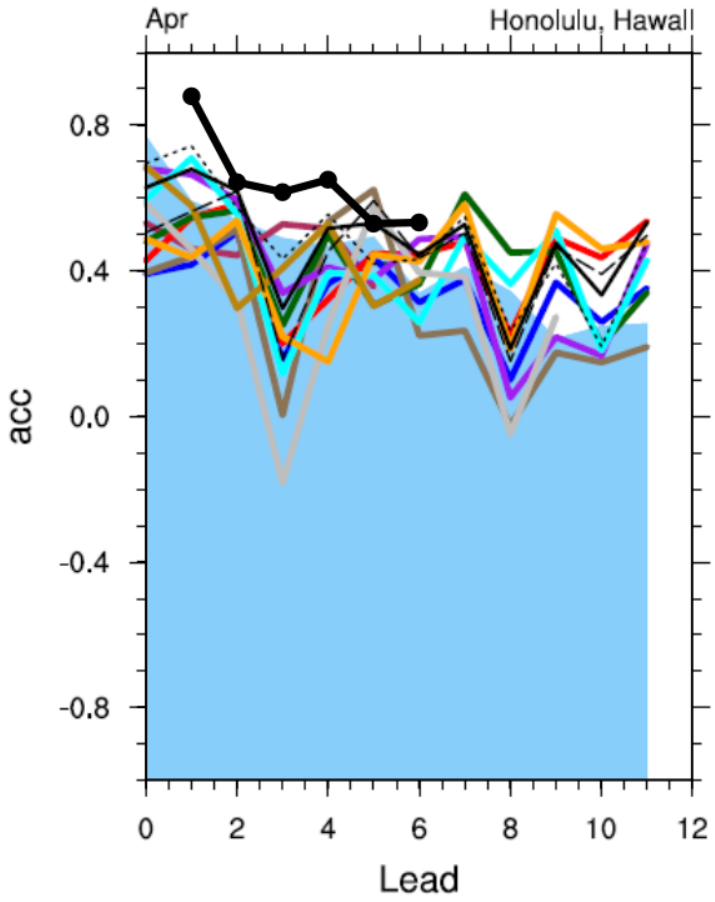

Figure 5.8: Monthly sea level forecast skill (anomaly correlation coefficient, acc) of dynamical models (colored lines) and observation-based sea level forecasts (black line with dots) compared against damped persistence (light blue filled) initiated in April. Skill assessment of dynamical forecast models was provided via personal communication with Xiaoyu Long and Matthew Widlansky.

For most lead months available for the observation-based sea level forecast, the observation-based forecast was able to demonstrate forecast skills higher than the dynamical models. At 5-month lead, a few dynamical models exhibited slightly higher skill than the observation-based forecast. Regardless, the skill of the observation-based forecast exceeds the skill of the baseline damped persistence (blue shading) and a majority of the dynamical models at all lags. Given the simplicity of the observation-based forecasts, the results of this comparison are eye opening and highlight the importance of initial conditions when forecasting sea level. The observation-based forecasts are initialized directly from altimetry observations alone, which is not the case for the dynamical forecast systems.

5.4 Applicability of the observation-based sea level forecast in other Pacific Islands

This study focused on the Hawaiian Islands, however, the observation-based sea level forecast may also have utility for other Pacific Islands. Similar to Hawaii, coastal flooding at other tropical Pacific Islands often occurs when positive sea level anomalies coincide with high tides. Studies document that vast areas of the western Pacific are experiencing sea level rise, and the risk of coastal flooding at the Pacific Islands will increase further (e.g., *Merrifield and Maltrud*, 2011; *Perrette et al.*, 2013). Similar to the Hawaiian Islands, sea level rise will make such island locations more vulnerable to these extreme events and also high tide flooding events that cause nuisance flooding.

The observation-based sea level forecast shows utility in the Hawaiian Islands despite substantial mesoscale variability that makes forecasting sea level challenging. Other Pacific Islands, such as Johnston Island may find more useful skill in the mesoscale spatial scales, as it is located west of the Hawaiian Islands and in the path of the well known eddy generation region lee of the Island of Hawaii (Figure 2.4, Figure 4 in *Holland and Mitchum*, 2001). Pacific Islands located at lower latitudes expereince less mesoscale variability and could

potentially derive better skill and more utility from the observation-based sea level forecast (e.g., the forecasted long-period sea level could be added to predicted tides for near-real-time forecasts). Overall, there is potential for utility in the observation-based sea level forecast in the other Pacific Island locations, and it is suggested to expand the forecast locations to assess the skill of the sea level forecast for other locations in the Pacific.

5.5 Summary

Numerous high sea level events in summer 2017 attracted media, stakeholders, and public interest, which highlighted the need to better predict sea level and increase preparedness for such events in the future. As open-ocean sea level anomalies typically propagate east to west, the purpose of this work was to leverage the propagation and create efficient seasonal observation-based sea level forecasts for the Hawaiian Islands. The observation-based model was developed, in part, because operational dynamical models tend to have limited skill in forecasting sea level, particularly at mid-to-high latitudes, including the Hawaiian Islands.

The timescales for which open-ocean sea level can be used to forecast coastal sea level were assessed by spectral analysis and time series comparison between tide gauge and altimetry data. Results suggested that open-ocean sea level variability at periods longer than 30 days is clearly related to coastal sea level in Hawaii, and forecasts were generated using low-frequency tide gauge and altimetry sea level. It is important to realize that about 40% of daily mean coastal sea level variability occurs at periods shorter than 30 days, and this variability is omitted from the observation-based sea level forecast using the open-ocean altimetry data (Table 2.1). The lack of spectral coherence between open-ocean and coastal sea level at these periods does not mean that open-ocean anomalies with time scales shorter than 30 days do not affect coastal sea level, but that the dynamics are likely more complicated (e.g., likely impacting coastal trapped waves), and one cannot make a one-to-one relationship between open-ocean and coastal sea level.

An optimized observation-based forecast was created from weighted combinations of persistence and independent propagation-based forecasts for large (>300 km) and mesoscale (<300 km) open-ocean anomalies. The observation-based sea level forecasts consistently exhibit higher skill than the baseline persistence forecast at long lead times out to 180 days. Evaluating over many training-validation sets shows that the weights assigned to each forecast component and the skill of the forecasts are robust and not sensitive to the particular subset of altimetry data used to train the forecast model. Our hypothesis was that the large-scale variability will exhibit greater predictability due to its coherency in time and zonal propagation. Our hypothesis was correct that, for the Hawaiian Islands in general, the forecasts are dominated by the large-scale component, while the mesoscale component received little weight in the optimized forecast. Operationally, the variance of the weights assigned to each forecast component varied little across training sets, and operational observation-based sea level predictions could simply use the median weights with no appreciable loss in skill. Finally, there was minimal significance in adding seasonal differences for speeds and weights in the sea level forecasts. For the Hawaiian Islands, the recommended observation-based sea level forecast is to use non-seasonal persistence and large-scale forecast with the median weights for the components.

The utility of the observation-based sea level forecast was demonstrated by pairing the mean sea level forecast with a statistical model relating mean sea level to counts of flooding threshold exceedances. Our second hypothesis was that coastal sea level at Hilo will be more predictable than Honolulu. The combined model performed exceedingly well in hindcasting seasonal periods of enhanced high-tide flooding at Hilo, underscoring the benefit of economical seasonal forecasts of mean sea level. Stakeholders can utilize the combined mean sea level and exceedance forecast model to assess flooding risks months in advance for facilitating preparedness across economic and coastal management sectors. The full potential has not yet been realized, but this work serves as a proof-of-concept with promising results for many stakeholders in coastal communities around the Hawaiian Islands.

Numerous assumptions were made to simplify the forecast methodology and make the sea level model as economical as possible. In future studies, relaxing some of these assumptions may increase the skill and utility of the observation-based sea level forecast. Most important would be to relax the assumption of purely zonal propagation and allow anomalies in different latitudes to factor into the forecast. This could be particularly effective at locations such as Honolulu where mesoscale anomalies formed in the lee of the islands are observed to propagate along the island chain, affecting Honolulu sea level before turning west into the basin. Another component of the forecast that could be improved is the propagation speed itself. The current observation-based sea level forecast assumes that one propagation speed per latitude for all lead-days. The propagation speed does vary as sea level anomalies propagate towards the island and interact with the bathymetry of the ridge (Figure 2.2). Allowing the speed to vary along the path of propagation could increase skill for both spatial scales.

References

Anderson, T. R., C. H. Fletcher, M. M. Barbee, L. N. Frazer, and B. M. Romine (2015), Doubling of coastal erosion under rising sea level by mid-century in Hawaii, *Natural Hazards*, *78*(1), 75–103.

Anderson, T. R., C. H. Fletcher, M. M. Barbee, B. M. Romine, S. Lemmo, and J. Delevaux (2019), Modeling multiple sea level rise stresses reveals up to twice the land at risk compared to strictly passive flooding methods (vol 8, 14484, 2018), *SCIENTIFIC REPORTS*, *9*.

APDRC (n.d.), Asia-Pacific Data-Research Center of the IPRC, `http://apdrc.soest.hawaii.edu`, (Accessed on 08/09/2020).

Caccamise, D. J., M. A. Merrifield, M. Bevis, J. Foster, Y. L. Firing, M. S. Schenewerk, F. W. Taylor, and D. A. Thomas (2005), Sea level rise at Honolulu and Hilo, Hawaii: GPS estimates of differential land motion, *Geophysical Research Letters*, *32*(3).

Chelton, D. B., and M. G. Schlax (1996), Global observations of oceanic Rossby waves, *Science*, *272*(5259), 234–238.

Chen, S., and B. Qiu (2010), Mesoscale eddies northeast of the Hawaiian archipelago from satellite altimeter observations, *Journal of Geophysical Research: Oceans*, *115*(C3).

Church, J. A., et al. (2013), Sea level change. Climate change 2013: The physical science basis. Contribution of working group I to the fifth assessment report of the intergovernmental panel on climate change, *Cambridge University Press, Cambridge, United Kingdom and New York, NY, USA*, pp. 1137–1216.

Cushman-Roisin, B., and J.-M. Beckers (2011), *Introduction to geophysical fluid dynamics: physical and numerical aspects*, Academic press.

DBEDT (2020), Visitor statistics, `https://dbedt.hawaii.gov/visitor/`, (Accessed on 08/05/2020).

DLNR (2017), Anticipated "king tides" merit watchful preparation, opportunity for 'citizen science' observations, https://dlnr.hawaii.gov/blog/2017/05/25/nr17-085/, (Accessed on 08/05/2020).

EPA (2019), King tides and climate change, https://www.epa.gov/cre/king-tides-and-climate-change, (Accessed on 08/05/2020).

Firing, Y. L., and M. A. Merrifield (2004), Extreme sea level events at Hawaii: Influence of mesoscale eddies, *Geophysical Research Letters*, *31*(24).

Fletcher, C. H., R. Boyd, W. J. Neal, and V. Tice (2010), *Living on the shores of Hawaii: Natural hazards, the environment, and our communities*, University of Hawaii Press.

Fu, L.-L., and B. Qiu (2002), Low-frequency variability of the North Pacific Ocean: The roles of boundary-and wind-driven baroclinic Rossby waves, *Journal of Geophysical Research: Oceans*, *107*(C12), 13–1.

Gill, A., J. Green, and A. Simmons (1974), Energy partition in the large-scale ocean circulation and the production of mid-ocean eddies, *Deep sea research and oceanographic abstracts*, *21*(7), 499–528.

Glazman, R. E., and P. B. Weichman (2005), Meridional component of oceanic Rossby wave propagation, *Dynamics of atmospheres and oceans*, *38*(3-4), 173–193.

Habel, S., C. H. Fletcher, T. R. Anderson, and P. R. Thompson (2020), Sea-level rise induced Multi-Mechanism flooding and contribution to urban infrastructure failure, *Scientific reports*, *10*(1), 1–12.

HNN (2019), Another round of king tides, south swell triggers coastal flooding concerns, https://www.hawaiinewsnow.com/2019/07/02/its-that-time-year-again-king-tides-are-returning-hawaii-shores/, (Accessed on 08/05/2020).

Holland, C. L., and G. T. Mitchum (2001), Propagation of big island eddies, *Journal of Geophysical Research: Oceans*, *106*(C1), 935–944.

Kiernan, D. (2014), *Natural resources biometrics*, SUNY Textbooks.

LeBlond, P. H., and L. A. Mysak (1981), *Waves in the ocean*, Elsevier.

Lindo-Atichati, D., Y. Jia, J. L. Wren, A. Antoniades, and D. R. Kobayashi (2020), Eddies in the Hawaiian Archipelago Region: Formation, characterization, and potential implications on larval retention of reef fish, *Journal of Geophysical Research: Oceans*, *125*(5), e2019JC015,348.

Long, X., M. J. Widlansky, F. Schloesser, P. R. Thompson, H. Annamalai, M. A. Merrifield, and H. Yoon (2020), Higher sea levels at Hawaii caused by strong El Niño and weak trade winds, *Journal of Climate*, *33*(8), 3037–3059.

Lumpkin, R., and P. Flament (2001), Lagrangian statistics in the central North Pacific, *Journal of marine systems*, *29*(1-4), 141–155.

McDonald, N. R. (1999), The motion of geophysical vortices, *Philosophical Transactions of the Royal Society of London. Series A: Mathematical, Physical and Engineering Sciences*, *357*(1763), 3427–3444.

Merrifield, M. A., and M. E. Maltrud (2011), Regional sea level trends due to a Pacific trade wind intensification, *Geophysical Research Letters*, *38*(21).

Mori, S. (2017), Strange Waikiki, Hawaii! "king tides" causing flooding crisis, `https://news.yahoo.co.jp/byline/morisayaka/20170525-00071294/`, (Accessed on 08/05/2020).

Müller, P., and H. von Storch (2004), *Computer modelling in atmospheric and oceanic sciences*, Springer.

NOAA (n.d.a), Datums - NOAA Tides & Currents, `https://tidesandcurrents.noaa.gov/datums.html`, (Accessed on 08/06/2020).

NOAA (n.d.b), CO-OPS API for data retrieval, `https://api.tidesandcurrents.noaa.gov/api/prod/`, (Accessed on 08/09/2020).

NOAA (n.d.c), What are harmonic constituents? - NOAA Tides & Currents, `https://tidesandcurrents.noaa.gov/about_harmonic_constituents.html`, (Accessed on 08/06/2020).

Perrette, M., F. Landerer, R. Riva, K. Frieler, and M. Meinshausen (2013), A scaling approach to project regional sea level rise and its uncertainties, *Earth System Dynamics*, *4*(1), 11–29.

Qiu, B. (1999), Seasonal eddy field modulation of the North Pacific Subtropical Countercurrent: TOPEX/Poseidon observations and theory, *Journal of Physical Oceanography*, *29*(10), 2471–2486.

Rotzoll, K., and C. H. Fletcher (2013), Assessment of groundwater inundation as a consequence of sea-level rise, *Nature Climate Change*, *3*(5), 477–481.

SankeiBiz (2017), "Living with the water" king tides attacking the world: Record breaking flooding in May Waikiki in 112 years, https://www.sankeibiz.jp/smp/compliance/news/170710/cpd1707100500004-s2.htm, (Accessed on 08/05/2020).

Schureman, P. (1941), *Manual of harmonic analysis and prediction of tides*, 98, US Government Printing Office.

Sea Grant Program (2018), Hawai'i and Pacific Islands king tides project, https://seagrant.soest.hawaii.edu/coastal-and-climate-science-and-resilience/ccs-projects/what-is-a-king-tide/, (Accessed on 08/05/2020).

Taherkhani, M., S. Vitousek, P. L. Barnard, N. Frazer, T. R. Anderson, and C. H. Fletcher (2020), Sea-level rise exponentially increases coastal flood frequency, *Scientific reports*, *10*(1), 1–17.

Thompson, P. R., M. J. Widlansky, M. A. Merrifield, J. M. Becker, and J. J. Marra (2019), A statistical model for frequency of coastal flooding in Honolulu, Hawaii, during the 21st century, *Journal of Geophysical Research: Oceans*, *124*(4), 2787–2802.

Widlansky, M. J., et al. (2017), Multimodel ensemble sea level forecasts for tropical Pacific Islands, *Journal of Applied Meteorology and Climatology*, *56*(4), 849–862, doi:10.1175/JAMC-D-16-0284.1.

Wyrtki, K., L. Magaard, and J. Hager (1976), Eddy energy in the oceans, *Journal of Geophysical Research*, *81*(15), 2641–2646.

Yang, L., and O. P. Francis (2019), Sea-level rise and vertical land motion on the Islands of Oahu and Hawaii, Hawaii, *Advances in Space Research*, *64*(11), 2221–2232.

Yoon, H., M. J. Widlansky, and P. R. Thompson (2018), Nu'a Kai: Flooding in Hawaii caused by a "stack" of oceanographic processes [in "State of the Climate in 2017"], *Bulletin of the American Meteorological Society*, *99*(8), S88–S89.

Yoshida, S., B. Qiu, and P. Hacker (2010), Wind-generated eddy characteristics in the lee of the island of Hawaii, *Journal of Geophysical Research: Oceans*, *115*(C3).